

On the onset of high-Reynolds-number grid-generated wind tunnel turbulence

By L. MYDLARSKI AND Z. WARHAFT

Sibley School of Mechanical and Aerospace Engineering, Cornell University, Ithaca, NY 14853, USA

(Received 6 November 1995 and in revised form 25 March 1996)

Using an active grid devised by Makita (1991), shearless decaying turbulence is studied for the Taylor-microscale Reynolds number, R_λ , varying from 50 to 473 in a small ($40 \times 40 \text{ cm}^2$ cross-section) wind tunnel. The turbulence generator consists of grid bars with triangular wings that rotate and flap in a random way. The value of R_λ is determined by the mean speed of the air (varied from 3 to 14 m s^{-1}) as it passes the rotating grid, and to a lesser extent by the randomness and rotation rate of the grid bars. Our main findings are as follows. A weak, not particularly well-defined scaling range (i.e. a power-law dependence of both the longitudinal (u) and transverse (v) spectra, $F_{11}(k_1)$ and $F_{22}(k_1)$ respectively, on wavenumber k_1) first appears at $R_\lambda \sim 50$, with a slope, n_1 , (for the u spectrum) of approximately 1.3. As R_λ was increased, n_1 increased rapidly until $R_\lambda \sim 200$ where $n \sim 1.5$. From there on the increase in n_1 was slow, and even by $R_\lambda = 473$ it was still significantly below the Kolmogorov value of 1.67. Over the entire range, $50 \leq R_\lambda \leq 473$, the data were well described by the empirical fit: $n_1 = \frac{5}{3}(1 - 3.15R_\lambda^{-2/3})$. Using a modified form of the Kolmogorov similarity law: $F_{11}(k_1) = C_{1*}\varepsilon^{2/3}k_1^{-5/3}(k_1\eta)^{5/3-n_1}$ where ε is the turbulence energy dissipation rate and η is the Kolmogorov microscale, we determined a linear dependence between n_1 and C_{1*} : $C_{1*} = 4.5 - 2.4n_1$. Thus for $n_1 = 5/3$ (which extrapolation of our results suggests will occur in this flow for $R_\lambda \sim 10^4$), $C_{1*} = 0.5$, the accepted high-Reynolds-number value of the Kolmogorov constant. Analysis of the p.d.f. of velocity differences $\Delta u(r)$ and $\Delta v(r)$ where r is an inertial subrange interval, conditional dissipation, and other statistics showed that there was a qualitative difference between the turbulence for $R_\lambda < 100$ (which we call weak turbulence) and that for $R_\lambda > 200$ (strong turbulence). For the latter, the p.d.f.s of $\Delta u(r)$ and $\Delta v(r)$ had super Gaussian tails and the dissipation (both of the u and v components) conditioned on $\Delta u(r)$ and $\Delta v(r)$ was a strong function of the velocity difference. For $R_\lambda < 100$, p.d.f.s of $\Delta u(r)$ and $\Delta v(r)$ were Gaussian and conditional dissipation statistics were weak. Our results for $R_\lambda > 200$ are consistent with the predictions of the Kolmogorov refined similarity hypothesis (and make a distinction between the dynamical and kinematical contributions to the conditional statistics). They have much in common with similar statistics done in shear flows at much higher R_λ , with which they are compared.

1. Introduction

We address here, from an experimental viewpoint, the way in which the characteristics of turbulence, particularly its spectrum and probability density function, evolve

as the Reynolds number is varied from low to high values. The flow is shearless grid turbulence and due to the novel active grid design of Makita (1991), a Taylor microscale Reynolds number ($R_\lambda \equiv u\lambda/\nu$, where u is the longitudinal r.m.s. velocity, λ is the Taylor microscale and ν is the kinematic viscosity) of nearly 500 is achieved. In particular, our aim is to determine at what R_λ high-Reynolds-number turbulence (in the Kolmogorov sense) first occurs in such a flow.

The central postulate of the Kolmogorov (1941*a, b*) phenomenological theory of turbulence is that if the Reynolds number is sufficiently high, there is a range of scales that are locally isotropic. Here there exists a scaling region, known as the inertial subrange, that separates the low-wavenumber region (large scales) which are affected by initial and boundary conditions and are therefore not universal, from the very high-wavenumber region of the spectrum, in which viscous dissipation occurs (Batchelor 1953; Monin & Yaglom 1975; Lesieur 1990). Within the inertial subrange, the Kolmogorov (1941, referred to herein as K41) theory predicts that the second-order structure function should vary as $r^{2/3}$, where r is the separation distance between two points. By means of a Fourier transformation, this result may be more familiarly expressed in terms of the one-dimensional spectra in the form

$$F_{11}(k_1) = C_1 \varepsilon^{2/3} k_1^{-5/3}, \quad (1)$$

$$F_{22}(k_1) = F_{33}(k_1) = C_2 \varepsilon^{2/3} k_1^{-5/3}. \quad (2)$$

Here $F_{11}(k_1)$, $F_{22}(k_1)$ and $F_{33}(k_1)$ are respectively the streamwise power spectra of the longitudinal velocity fluctuations, u , and the transverse velocity fluctuations, v and w , k_1 is the longitudinal wavenumber, ε is the turbulence energy dissipation rate per unit mass (defined below) and C_1 and C_2 are the Kolmogorov constants (Monin & Yaglom 1975). Since the Kolmogorov theory assumes local isotropy, it can be deduced from (1) and (2) on purely kinematical grounds that $C_2/C_1 = 4/3$.

For equations (1) and (2) to hold, the Reynolds number must be high. Yet it is well known that three-dimensional turbulence, exhibiting a multiplicity of scales, can exist at Reynolds numbers that are too low to have the $-5/3$ scaling region. Thus traditional grid-generated turbulence (e.g. Comte-Bellot & Corrsin 1971) with an R_λ of around 50 does not have a scaling region, but is sufficiently well developed so that the dissipation rate can be estimated by the scaling law

$$\varepsilon = A \langle u^2 \rangle^{3/2} / \ell. \quad (3)$$

Here, ℓ is the turbulence integral scale (defined below), A is a constant close to unity and the angle brackets denote averaging. This law implies a cascade since the dissipation (a small-scale phenomenon) is determined from the large-scale energetics, and the viscosity does not appear explicitly. It has been shown that even in low-Reynolds-number grid turbulence (see for example Sirivat & Warhaft 1983, figure 5) ε determined from (3) is close to the model-independent estimate (assuming only isotropy at the dissipation scales) given by

$$\varepsilon = 15\nu \langle (\partial u / \partial x)^2 \rangle \quad (4)$$

where $\partial u / \partial x$ is the streamwise derivative of the longitudinal velocity fluctuations. Does such low-Reynolds-number turbulence differ qualitatively from that at high-Reynolds-number? And if so, what are discernible differences? Finally, at what R_λ does the low-Reynolds-number turbulence, without a scaling region, undergo transition to high-Reynolds-number turbulence?

In order to answer these questions, it appears that the Reynolds number should be varied from low to high values in a systematic way using the same type of initial and boundary conditions. Moreover, ideally the turbulence should be shearless and homogeneous, and preferably isotropic at all scales. If it is only locally isotropic (with large-scale anisotropy imposed by the boundary conditions), then below a certain Reynolds number the whole spectrum will be anisotropic (and hence it will be affected by its boundary conditions) since there will not be a broad enough wavenumber range to allow the development of local isotropy. The recent boundary layer measurements of Saddoughi & Veeravalli (1994, referred to herein as S & V), indicate that not until $R_\lambda \sim 600$, a very high value in terms of laboratory flows, does a significant locally isotropic region of the spectrum develop. Below this the spectrum is affected by the Reynolds shear stress up to dissipation wavenumbers and there is little, if any, region of local isotropy. While these shear flow measurements clearly confirm Kolmogorov's hypothesis that at sufficiently high Reynolds number a locally isotropic region does exist, they are unable to examine the characteristics of isotropic turbulence at lower Reynolds numbers. To do this, grid-generated turbulence is ideally suited since it has no shear (and hence no Reynolds shear stress spectrum) and although the large-scale field is not quite isotropic, it is much closer to isotropy than that of shear flows (see §3).

The traditional method of generating (approximately) isotropic turbulence is by means of a grid: a rectangular array of (usually square sectioned) bars placed at the entrance of the test section (Batchelor 1953; Comte-Bellot & Corrsin 1966). As mentioned above, the R_λ is low, typically in the range 50 to 150, although there are some isolated results at high R_λ †. The reason for this is that grids produce low-intensity turbulence; the ratio of the r.m.s. to mean velocity, u/U , is generally 2% or less in the downstream region where the flow has reached isotropy. On the other hand, high R_λ can be easily obtained in shear flows because of their high intensities (jets, for example, have u/U of around 25%, e.g. Townsend 1976). In order to produce high- R_λ grid turbulence, the grid mesh must be large and so too must be the mean speed. The former requires extremely large tunnels since the tunnel must be many meshes wide to provide isotropy, the latter gives rise to probe resolution problems and to unwanted compressibility effects.

Many years ago, Corrsin suggested placing propellers on the grid to increase the turbulence intensity, but apparently he did not implement it (J. Lumley, private communication). Gad el Hak & Corrsin (1974) did publish work on a grid with attached jets, but this only modestly increased the R_λ . There have been other attempts (e.g. Ling & Wan 1972) to produce active grids, again with limited success. However, we recently became aware of a major advance by Makita and his colleagues at Toyohashi University of Technology (Makita *et al.* 1987; Makita & Sassa 1991; Makita 1991). They designed, constructed and tested an active bi-plane grid with randomly flapped agitator wings. Their results (most comprehensively described in Makita 1991) were particularly encouraging: in a tunnel of only $0.7 \times 0.7 \text{ m}^2$ and a mean velocity of 5 m s^{-1} , an R_λ of nearly 400 was achieved. The flow had good homogeneity and was shearless. The probability density functions (p.d.f.s) of the velocity field were well behaved and the spec-

† Kistler & Vrebalovich (1966) achieved an R_λ of over 500 in a massive wind tunnel built for aircraft research. Their results show a clear inertial subrange. However, there was no systematic variation of R_λ and many of the statistics relevant to the present work were not computed. The tunnel was dismantled soon after the measurements were made.

trum showed well over one decade of inertial subrange, of slope close to $-5/3$. The only slight drawback was that the anisotropy, u/v , was 1.22. This is a little higher than that of conventional grid turbulence which has values around 1.1 (Comte-Bellot & Corrsin 1967). This aspect, which we will see does not appear to affect the inertial-range dynamics, does preclude accurate determination of the three-dimensional spectrum from the u and v components, assuming isotropy of the large-scales.

Briefly, Makita places triangular agitator wings on each grid mesh. A regular pulse generator rotates the grid bars (and hence the wings) and at the same time the motor is fed a random pulse which reverses the rotation of the grid bar. Thus the wing, always in rotational motion, reverses its direction randomly, providing a flapping motion. Each bar is separately controlled, providing random flapping between bars. The resultant turbulence has high intensity (up to 15%) and an integral scale larger than the mesh (rather than smaller produced by conventional grids). Both act to produce the high R_λ .

We decided to build a Makita-style active grid in order to study scalar mixing at high-Reynolds-numbers. Our preliminary experiments led us to explore the questions raised above concerning the evolution of grid turbulence with Reynolds number, and this is the subject of the present work. Results on scalar mixing are in preparation.

Our objective, then, is to study the evolution of grid-generated turbulence with R_λ . In particular we wish to determine whether we can produce high-Reynolds-number turbulence in a laboratory-scale wind tunnel that has characteristics similar to those measured at high-Reynolds-number in the atmosphere and oceans, but without the complicating effects of shear. If this can be achieved then we may address many questions concerning the fine-scale structure that cannot be properly studied in the uncontrolled environment.

The outline of the work is as follows. After describing the apparatus in §2 and the grid performance in §3, we examine the nature of the velocity spectra over the R_λ range 50 to nearly 500 in §4. Emphasis is placed on how the magnitude of the scaling exponent, n , and thus the Kolmogorov ‘constant’, varies with R_λ . We then turn to an examination of the p.d.f. and conditional dissipation of velocity differences determined over inertial subrange intervals. These results are discussed in terms of the internal intermittency of the flow and are related to recent investigations in shear flows.

2. Apparatus

The experiments were conducted in our vertical wind tunnel which has a 40.65×40.65 cm² cross-section and is 4.5 m, long (see Sirivat & Warhaft 1983 for a sketch). At the entrance of the test section, we replaced the conventional static grid with an active grid. Our design follows that of Makita (1991) although there are some variations. A sketch with dimensions is shown in figure 1(a) and a photo of the grid in the tunnel test section is shown in figure 1(b). The basic operation of the grid has been outlined in the Introduction. Here we provide its specifications. The mesh spacing, M , between the grid bars is 5 cm, providing a tunnel cross-section of $8 \times 8 M$. Each of the 14 grid bars is a 0.64 cm diameter aluminium rod with 0.38 mm thick aluminium wings, attached as shown in figure 1(a). Every rod is independently driven by a Superior Electric 5 W D.C. synchronous stepping motor (shown in the photo, figure 1b), with 200 steps per revolution. The rotation speed of the rods could be varied up to a maximum speed of about 4 revolutions per second

(r.p.s.), but for nearly all of the measurements reported here it was set to 2 r.p.s. (see §3). A random signal was fed into the motor to alter its rotation direction. The average time between switching was of the order of a rotation period. Thus sometimes a bar would undergo more than a full cycle before switching while other times it would only undergo a fraction of a cycle. The appearance of the whole grid when operating in this random mode was of a shimmering nature since all of the 14 rods were acting independently. (Note that all the wings are in the same plane along a particular grid bar. This aspect could also be randomized but we have not done so.)

The grid was also operated in what we call a synchronous mode. Here, the random switching was not used and the initial condition was that all of the North-South wings were horizontal and all of the East-West wings were vertical. Their relative orientation did not change over the measurement duration. (Their rotation direction was reversed on alternate rods so as not to add net vorticity.) The main difference between the random and synchronous modes was that the latter produced a lower turbulence intensity and a smaller longitudinal integral scale (and thus a lower R_λ for the same mean wind tunnel speed). Moreover, because of the synchronous rotation, the low-wavenumber energy-containing region of the spectrum was more contaminated by the grid bar rotation frequency (see §3) and thus most of our results in this paper focus on the random mode. (On the other hand, the synchronous mode was found to be better behaved than the random mode for the investigation of passive scalars, probably due to the smaller integral scale. This is the subject of a future paper.) Apart from these differences in performance, the nature of the results were similar for the grid operated in either mode. Thus, spectral slopes and p.d.f.s were similar when the Reynolds number was the same.

The tunnel speed was varied from 3 m s^{-1} to 14 m s^{-1} giving a variation in R_λ from 99 to 473. (Some supplementary measurements at $R_\lambda = 50$ and 100 were done using conventional static grids.) The rate of rotation of the grid bars only slightly affected the turbulence level or R_λ . More significantly, it did produce a small spike in the spectrum at twice its rotation frequency (see §3).

To obtain good horizontal homogeneity in the velocity field, the grid had to be carefully tuned. Initially there was a large velocity deficit near the walls. Holes were drilled in the wings adjacent to the walls to reduce this. (These 'half' wings were attached to the frame of the grid and did not rotate, see figure 1a.) Notice that in figure 1(b) there appear to be holes also in the rotating wings. All of these (excepting those on the grid bars closest to the walls (figure 1a)) were taped over for the experiments to be described below. The mean velocity profiles will be discussed in the next section.

The velocity field was measured with a TSI 1241 tungsten X-probe calibrated using the method due to Browne, Antonia & Chua (1989). Corroborative measurements for the u component were made with a single 'u' probe. The $3.2 \mu\text{m}$ tungsten wires with a length to diameter ratio of 200 were operated at an overheat ratio of 1.8 in conjunction with Dantec 55M01 constant-temperature anemometers. Tunnel and electronic noise (determined when there was no grid in the flow) was subtracted from the spectra on a mean-square basis. Wire end effect corrections were made using Wyngaard's (1968) method. All signals were low-pass filtered to eliminate high-frequency noise and digitized with a 12 bit A/D converter. Typically 4×10^5 samples were taken for each data record, rapidly for the spectra (order of a Kolmogorov time period) but slowly (order of an integral time period) for the p.d.f. measurements to provide statistical independence.

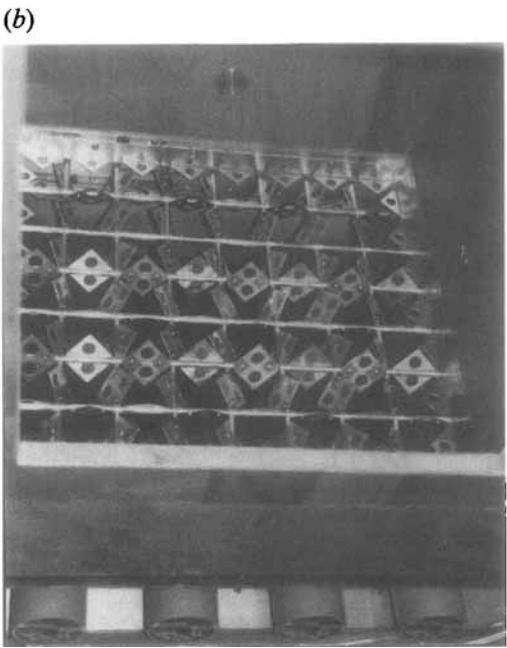
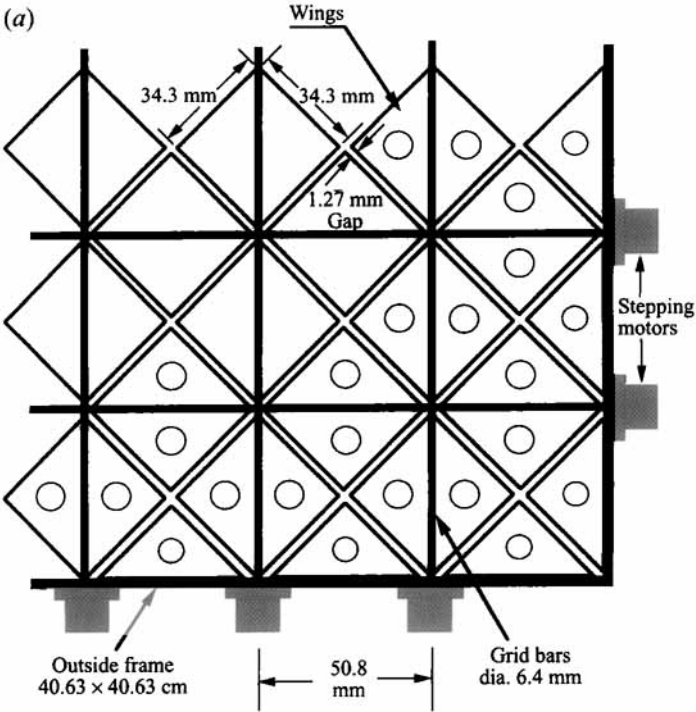


FIGURE 1. The active grid. (a) A sketch (not to scale). The circles represent holes in the wings, used to tune the flow so that it was close to horizontally homogeneous. The holes in the static wings (those attached to the tunnel wall) were 10.3 mm in diameter. Those in the rotating wings (attached to the grid bars) were of 11.9 mm diameter. (b) A photo of the grid. The tunnel is vertically oriented and the flow is upwards.

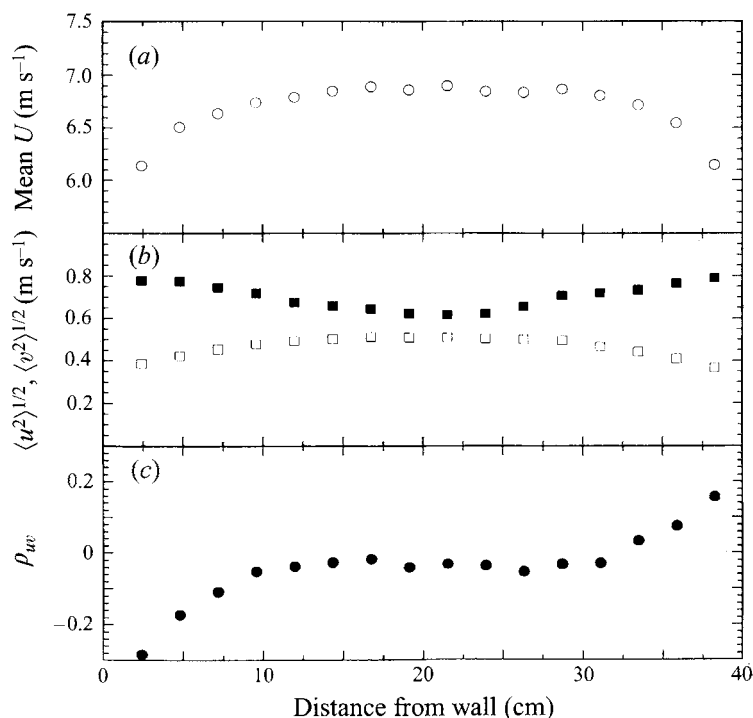


FIGURE 2. Mean (U), longitudinal and transverse r.m.s. profiles, $\langle u^2 \rangle^{1/2}$ (solid squares) and $\langle v^2 \rangle^{1/2}$ (open squares) respectively, and the cross-correlation coefficient between u and v , ρ_{uv} . $R_\lambda = 275$, random mode.

3. The grid performance

Before describing the main results concerning the evolution of the spectrum and p.d.f. with Reynolds number, we will outline the performance of the active grid, paying particular attention to its departure from 'ideal' grid-generated turbulence.

Cross-stream profiles of the mean speed, U , the root-mean-square longitudinal velocity and transverse velocity, $\langle u^2 \rangle^{1/2}$ and $\langle v^2 \rangle^{1/2}$ respectively, and the cross-correlation coefficient between u and v , $\rho_{uv} (\equiv \langle uv \rangle / [\langle u^2 \rangle^{1/2} \langle v^2 \rangle^{1/2}])$ where $\langle uv \rangle$ is the kinematic Reynolds stress) are shown in figure 2 for the grid run in random mode at 6.9 m s^{-1} ($R_\lambda = 275$). There is good homogeneity in U for nearly 20 cm in the transverse direction and there is no Reynolds stress for even a larger core than this. The r.m.s. u and v profiles curve in opposite directions giving quite strong anisotropy as the walls are approached. In the central core region $(\langle u^2 \rangle / \langle v^2 \rangle)^{1/2}$ is about 1.21. This result, which is consistent with that of Makita (1991), is higher than that of static grid experiments which yield values of 1.1 or slightly less (e.g. Sirivat & Warhaft 1983). We will return to this departure from isotropy in a moment. The profiles in figure 2 are typical of those done at other Reynolds numbers.

Figure 3 shows the decay of the longitudinal velocity variance and third moment as a function of x/M . Because of the large mesh ($M = 5 \text{ cm}$) and also because the test section had to be modified to accommodate the active grid, the test section was only $80M$ in extent. Nevertheless, the form of the variance decay law is similar to that observed in conventional grid-generated turbulence (e.g. Sirivat & Warhaft 1983). The decay law for $U = 6.7 \text{ m s}^{-1}$ was $\langle u^2 \rangle / U^2 = 1.23(x/M)^{-1.21}$. Nearly all of

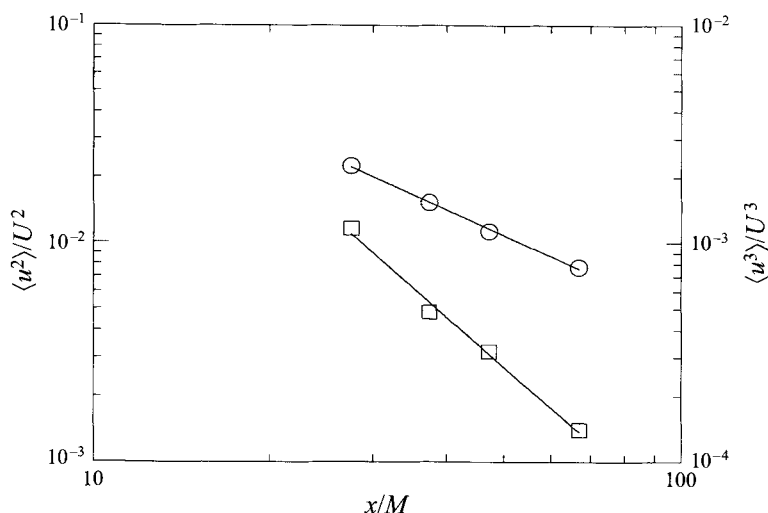


FIGURE 3. A typical longitudinal variance decay (circles) and third moment decay (squares). $U = 6.7 \text{ m s}^{-1}$, $R_\lambda = 319$ (at $x/M = 68$). For these measurements, done in the random mode, the bar rotation speed was 1 r.p.s. This produced a slightly higher R_λ (for the same mean speed) than did the higher rotation speed of 2 r.p.s., used for all the other measurements reported in this paper.

the measurements to be described in §4 were done at $x/M = 68$ where the turbulence intensity u/U was less than 10%. Table 1 lists a number of flow conditions and their relevant flow parameters. Typical u and v spectra for $u = 7.1 \text{ m s}^{-1}$ ($R_\lambda = 262$, random mode) are shown in figure 4. Unlike conventional grid turbulence they show a clear scaling region. Its extent and slope will be discussed in §4. Here we draw attention to the spikes at $k_1 = 3.5 \text{ m}^{-1}$. These are due to the rotation rate of the grid bars. In order not to contaminate the inertial-subrange dynamics we adjusted the grid bar rotation speed such that the spikes would occur at wavenumbers below those of the energy-containing scales. It was set to 2 r.p.s. for nearly all of the measurements reported here. (Changing the rotation speed slightly changed the value of R_λ but did not have a noticeable effect on the nature of the turbulence statistics.) The insert in figure 4 shows energy spectra determined by multiplying the power spectra by k_1 . Their peak provides a very good estimate of the integral scale of the turbulence (§4). They peak at $k_1 \sim 10 \text{ m}^{-1}$, well above the wavenumber of the spikes. For the case presented in figure 4 the spikes were responsible for 6% of the total r.m.s. This was fairly typical for the random mode of operation at other R_λ . (The values of $\langle u^2 \rangle$, R_λ , etc. in table 1 were determined with the effect of the spike subtracted from the spectrum on a mean-square basis.) Varying the grid bar rotation speed did not produce any noticeable change in the statistics of the velocity field for the inertial and dissipation ranges, providing we kept the spike at a lower wavenumber than the peak energy. This, and our observation that the synchronous mode gave results consistent with the random mode (although for a given mean speed the R_λ was lower) indicated that our results are relatively insensitive to the way we operated the grid. Moreover, when working at low R_λ , our active grid produced results consistent with conventional grid measurements (§4). Thus we do not believe the spikes contaminated the inertial- and dissipation-range statistics.

P.d.f.s of the u and v fluctuating components of velocity are shown in figure 5, for $U = 7.1 \text{ m s}^{-1}$ ($R_\lambda = 262$, random mode). For conventional grid turbulence, these

Speed (m s ⁻¹)	7.6		7.3		3.2		7.1		10.4		14.3	
	2.54 cm	Mesh	10.2 cm	Mesh	Synchronous	Random	Random	Random	Random	Random	Random	Random
Mode	60		60		68	68	68	68	68	68	68	68
x/M	0.0237		0.0266		0.0258	0.270	0.270	0.803	0.803	1.85	1.85	1.85
$\langle u^2 \rangle$ (m ² s ⁻²)	2.0		2.2		5.0	7.4	7.4	8.6	8.6	9.5	9.5	9.5
$\langle u^2 \rangle^{1/2} / U$ (%)	0.227		0.0708		0.0678	1.06	1.06	4.54	4.54	15.3	15.3	15.3
$\varepsilon (= 15\nu \int_0^\infty k_1^2 F_{11}(k_1) dk_1)$ (m ² s ⁻³)	0.0145		0.0551		0.0550	0.119	0.119	0.143	0.143	0.148	0.148	0.148
$\ell (= 0.9 \langle u^2 \rangle^{3/2} / \varepsilon)$ (m)	50		100		99	262	262	377	377	473	473	473
$R_\lambda (= \langle u^2 \rangle \{15/\nu/\varepsilon\}^{1/2})$	148		600		589	4130	4130	8520	8520	13400	13400	13400
$R_\eta (= \langle u^2 \rangle^{1/2} \ell / \nu)$	0.349		0.467		0.472	0.238	0.238	0.165	0.165	0.122	0.122	0.122
$\eta (= (\nu^3/\varepsilon)^{1/4})$ (mm)	1.3		1.3		1.40	1.54	1.54	1.56	1.56	1.58	1.58	1.58
n_1	1.1		1.3		—	1.45	1.45	1.52	1.52	1.56	1.56	1.56
n_2	0.57		0.55		—	0.54	0.54	0.53	0.53	—	—	—
$\langle (\partial u / \partial t)^2 \rangle / \langle (\partial v / \partial t)^2 \rangle$												

TABLE 1. Flow parameters. These six representative cases were selected from many more used to determine the flow evolution as a function of R_λ (see for example figure 10). The two lowest- R_λ cases were done using conventional static grids in our horizontal tunnel of cross-section area 91×91 cm² (Yoon & Warhaft 1990). The mesh M was 2.54 cm and 10.2 cm. The three highest- R_λ cases were done for the active grid in the random mode while for the measurements at $R_\lambda = 99$ the synchronous mode was used to compare with the measurements done with the static (10.2 cm) grid. n_1 and n_2 are the values of the scaling exponent for the u and v spectra respectively (see text, §4.1 for the way they were determined). The kinematic viscosity, ν , is 15×10^{-6} m² s⁻¹.

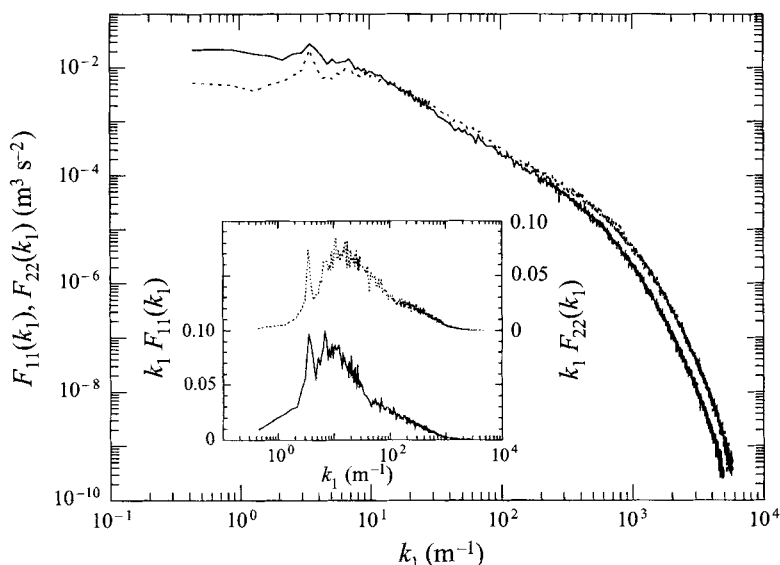


FIGURE 4. Longitudinal velocity spectrum, $F_{11}(k_1)$, solid line, and transverse spectrum, $F_{22}(k_1)$, dashed line. $R_\lambda = 262$, random mode. The insert shows $k_1 F_{11}(k_1)$ (solid line) and $k_1 F_{22}(k_1)$ (dashed line); k_1 is the longitudinal wavenumber $= 2\pi f/U$.

are Gaussian with the skewness $S_u (\equiv \langle u^3 \rangle / (\langle u^2 \rangle)^{3/2})$ and kurtosis $K_u (\equiv \langle u^4 \rangle / \langle u^2 \rangle^2)$ having values of 0 and 3 respectively. Here there are small departures: $S_u = 0.19$ and $K_u = 3.17$. For v , the skewness and kurtosis, S_v and K_v , were respectively 0.03 and 3.41. The relatively high turbulence intensity (table 1) and its rapid decay produces a small divergence of the turbulence kinetic energy, $\partial/\partial x_j (\frac{1}{2} \langle u_i u_i u_j \rangle)$. Although we determined this to be less than 5% of the turbulence energy dissipation rate ε , the existence of the triple moment induces a slight skewness in u . The experimentally derived law for the third moment is also plotted in figure 3. It is $\langle u^3 \rangle / U^3 = 2.58(x/M)^{-2.34}$ for $U = 6.7 \text{ m s}^{-1}$. This in turn possibly produces the small departure from the Gaussian state for v via higher-order terms in the equation for v^4 . Of course the skewness in v must be zero by symmetry and our results confirm this to a high degree. Although the large-scale velocity field is not strictly Gaussian we will show that its departure from the Gaussian state is very small compared to the highly non-Gaussian statistics of velocity differences and derivatives determined in the inertial subrange.

We now return to the departure from isotropy observed in the r.m.s. u and v profiles of figure 2. As noted in the Introduction, the anisotropic effects of shear flows are evident in the inertial subrange as well as at large-scales. Thus it is important to determine whether the anisotropy of this flow (which is much less than that observed in shear flows) affects the inertial subrange. Figure 6 shows the coherence between u and v in the laboratory coordinates and in transformed coordinates, with a 45° rotation. Here $u' = (u + v)/\sqrt{2}$ and $v' = (u - v)/\sqrt{2}$. In the laboratory coordinates, there is no coherence between u and v while with the 45° rotation there is coherence at low wavenumbers but this drops to zero by $k_1 \eta \sim 3 \times 10^{-3}$. (The cross-correlation coefficient between u' and v' was 0.21.) Also shown in figure 6 is the u spectrum compensated to produce a plateau in the scaling region (i.e. the inertial subrange, see §4.1). It is clear that the coherence between u and v is essentially zero by the time the inertial subrange begins. We note that the 45° rotation produced the largest

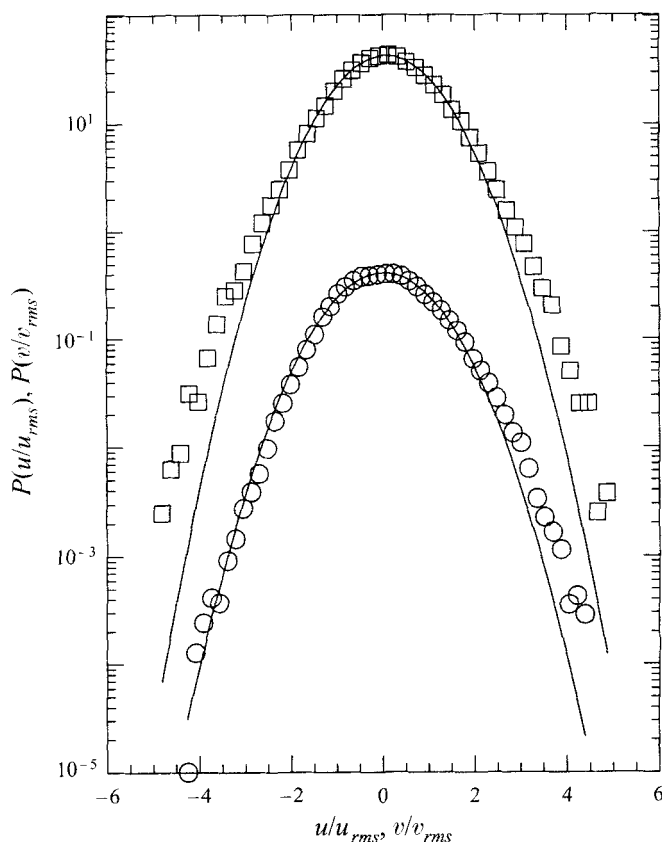


FIGURE 5. The u (circles) and v (squares) probability density functions. $S_u = 0.19$, $K_u = 3.17$; $S_v = 0.03$, $K_v = 3.41$. The v p.d.f. has been moved vertically 2 decades with respect to the u p.d.f. The solid curves are Gaussian. $R_\lambda = 262$, random mode.

coherence. By contrast, in shear flows the cross-spectrum of u and v (and hence its coherence) is significant well into the inertial subrange at these Reynolds numbers. (See for example figure 20 of Saddoughi & Veeravalli.)

In summary, the active grid is not quite as 'clean' as (lower Reynolds number) traditional passive grids, showing a greater departure from isotropy in the velocity field at the large-scales as well as having a small departure from strictly Gaussian p.d.f.s. However, the anisotropy appears to be strictly confined to the integral scales, making this grid well suited to an investigation of the behaviour of inertial-subrange structure.

4. Results

Our objective is to study the way grid turbulence evolves as a function of Reynolds number. The results are reported in terms of the spectra (§4.1) and the p.d.f.s and conditional statistics (§4.2). This categorization is useful since the classical formulation of the Kolmogorov similarity theory (K41) is in terms of spectra (or related second-order structure functions) while the details of the intermittent structure are best described in terms of the p.d.f.s and conditional statistics (Kolmogorov 1962, referred to herein as K62). Before we begin, however, we will outline the flow parametrization.

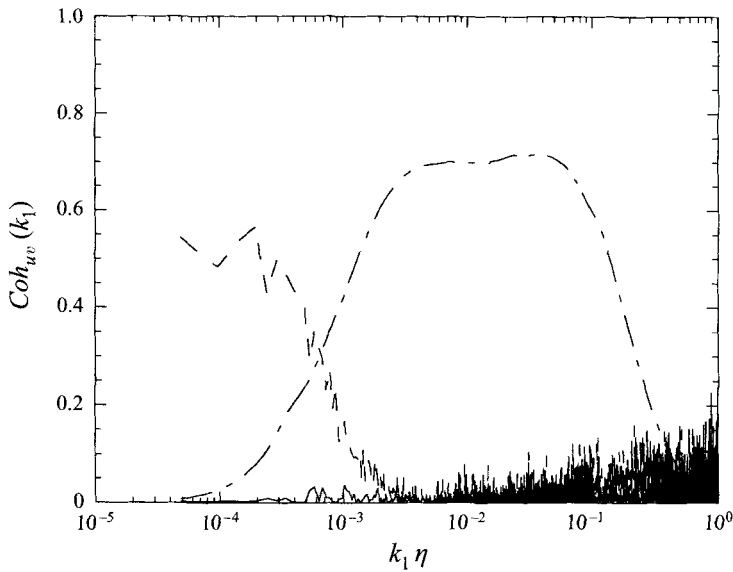


FIGURE 6. The coherence between u and v , Coh_{uv} . The solid line (essentially zero) is Coh_{uv} in laboratory coordinates. The dashed line is Coh_{uv} with the coordinate system rotated 45° with respect to the flow direction. The curve with the plateau is the compensated velocity spectrum to be discussed in §4.1. The plateau region is the inertial subrange.

We report our results in terms of the Taylor-microscale Reynolds number $R_\lambda (\equiv u\lambda/\nu)$ where the Taylor microscale is defined in the usual way as

$$\lambda = [\langle u^2 \rangle / \langle (\partial u / \partial x)^2 \rangle]^{1/2}. \quad (5)$$

The longitudinal velocity derivative in the streamwise direction was determined using the Taylor hypothesis $\partial(\quad)/\partial x = -U^{-1}\partial(\quad)/\partial t$. This is a very good approximation for this shearless flow with a relatively low turbulence intensity of (around 7%, table 1).

From equation (4) it follows that

$$\varepsilon = 15\nu \langle u^2 \rangle / \lambda^2. \quad (6)$$

Consistent with the findings of Sirivat & Warhaft (1983), the value of ε determined from (6) was within 5% of ε determined using the isotropic relations (Batchelor 1953)

$$\varepsilon = 15\nu \int_0^\infty k_1^2 F_{11}(k_1) dk_1 \quad (7)$$

$$= 7.5\nu \int_0^\infty k_1^2 F_{22}(k_1) dk_1. \quad (8)$$

In fact, for the values of λ and R_λ listed in table 1, λ was determined using equations (7) and (6), rather than directly, using equation (5). Another useful Reynolds number is based on the integral lengthscale, ℓ , and is defined as

$$R_\ell = u\ell/\nu. \quad (9)$$

There are various ways of defining ℓ (see e.g. Sirivat & Warhaft 1983). We determined it by finding the wavenumber at which the $k_1 F_{11}(k_1)$ spectrum peaked (see for example the inset of figure 4). Since there is scatter associated with this method, we correlated

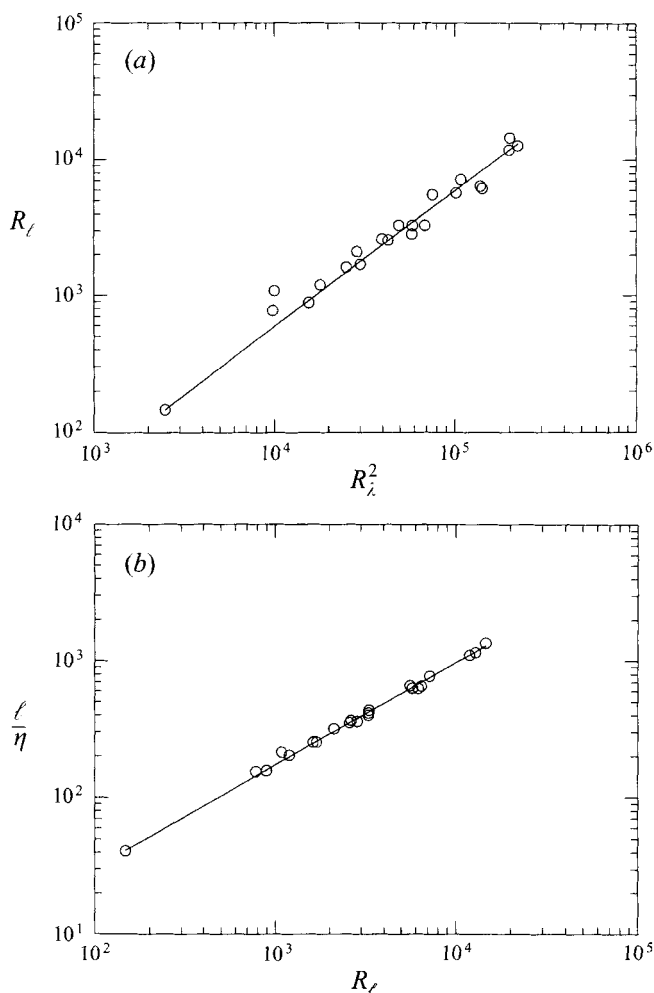


FIGURE 7. The relation between R_ℓ and R_λ . The data were obtained with the active grid and supplemented with use of a passive grid at low-Reynolds-number. (a) R_ℓ vs. R_λ^2 . The line is the best fit to $R_\ell = (A/15)R_\lambda^2$. (b) ℓ/η vs. R_ℓ .

R_ℓ with R_λ (which can be accurately determined). A plot of R_ℓ vs. R_λ^2 is shown in figure 7(a). From equations (3), (6) and (9) it follows that

$$R_\ell = (A/15)R_\lambda^2. \quad (10)$$

From the plot of figure 7(a) we determined A to be 0.9. Defining the Kolmogorov microscale η in the usual way as $(\nu^3/\varepsilon)^{1/4}$, equation (10) can be restated as

$$\ell/\eta = A^{1/4}R_\ell^{3/4}. \quad (11)$$

For reference a plot of this is shown in figure 7(b). The values of ℓ listed in table 1 have been determined using equation (3), with $A = 0.9$, i.e. we re-define ℓ (thereby eliminating the scatter) by

$$\ell = 0.9\langle u^2 \rangle^{3/2}/\varepsilon \quad (12)$$

where ε is determined from (7).

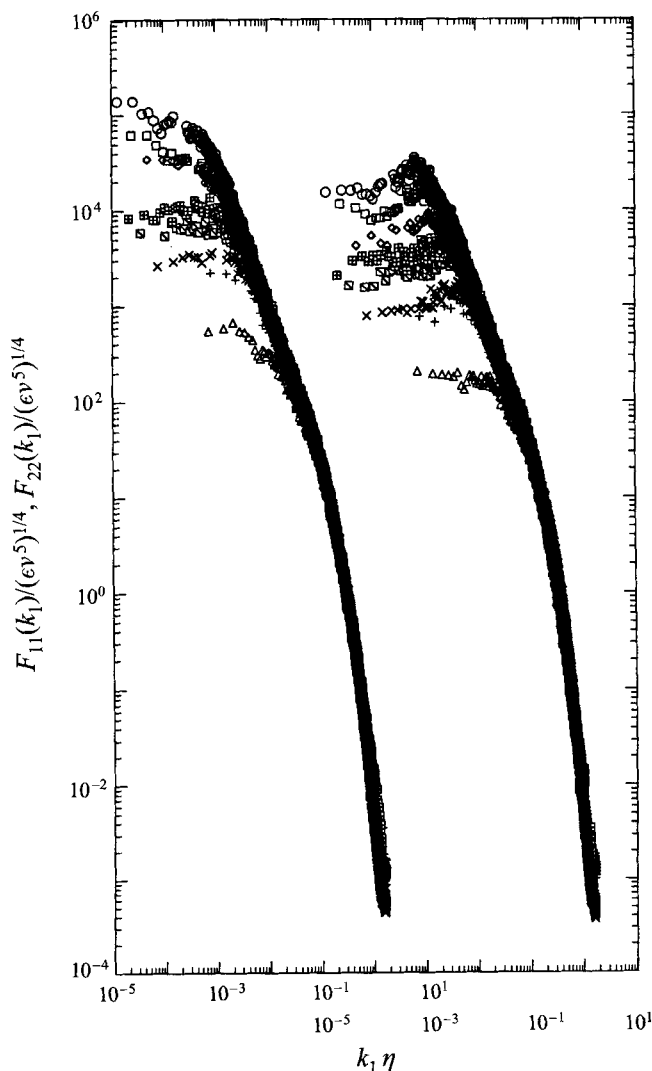


FIGURE 8. The u spectra (left-hand set) and v spectra for the various experiments. The symbols are as follows (R = random, S = synchronous): \bigcirc , $R_\lambda = 473$ R; \square , $R_\lambda = 330$ R; \diamond , $R_\lambda = 275$ R; \boxplus , $R_\lambda = 207$ S; \boxminus , $R_\lambda = 174$ S; \times , $R_\lambda = 124$ S; $+$, $R_\lambda = 100$ (conventional grid, $M = 10.2$ cm); \triangle , $R_\lambda = 50$ (conventional grid, $M = 2.54$ cm).

4.1. The spectra

Figure 8 shows the one-dimensional u and v power spectra. The R_λ range is from 50 to 473. The lowest R_λ measurements ($R_\lambda = 50$ and 100) were done with conventional static grids. All of the measurements at higher R_λ were done with the active grid operating either in the synchronous or random modes. Our results are similar (and have comparable scatter) to the recent compilation of S & V (their figure 9) which cover the R_λ range from 23 to 3,200. Such plots have provided strong support for K41 scaling.

A more stringent test for Kolmogorov scaling is to display the data in compensated form. Figure 9(a) shows the F_{11} spectra multiplied by $\varepsilon^{-2/3} k_1^{5/3}$. The inertial range should be horizontal on such a plot. The four representative compensated spectra are

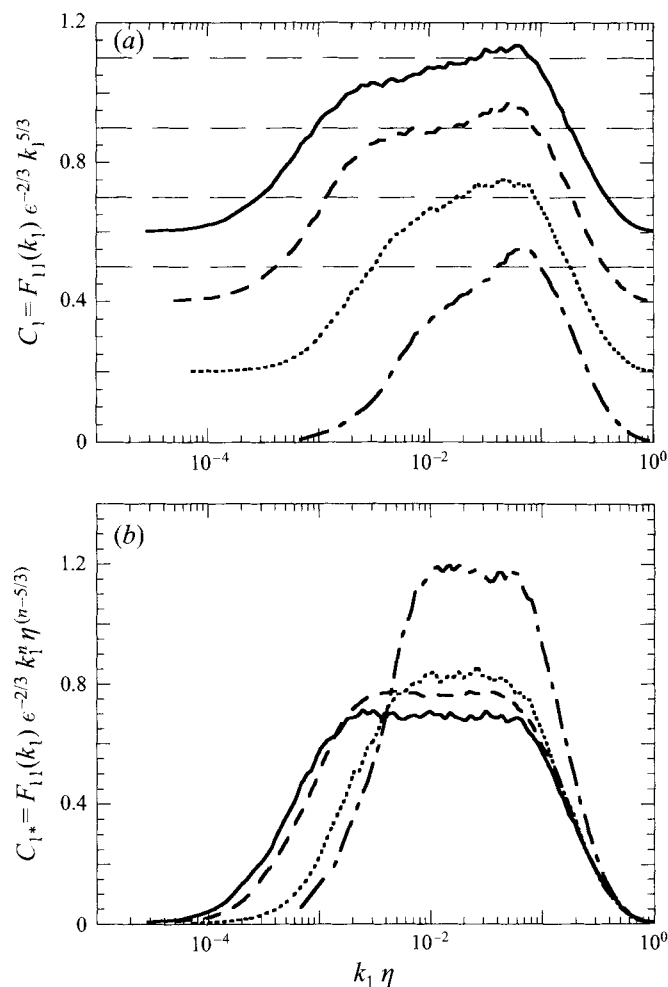


FIGURE 9. Compensated u spectra for $R_\lambda = 99, 199, 373$ and 448 , all done in the random mode except $R_\lambda = 99$ which was done in the synchronous mode. (a) $F_{11}(k_1) e^{-2/3} k_1^{5/3} = C_1$, (b) $F_{11}(k_1) e^{-2/3} k_1^n \eta^{(n-5/3)} = C_{1*}$. Each horizontal dashed line in (a) is 0.5, the accepted value for C_1 (equation (1)) for high-Reynolds-number turbulence. Each of the curves in (a) has been successively shifted by 0.2 with respect to the lower one. The Reynolds number increases from the bottom curve upwards in (a) and from the upper curve downwards in (b).

for $R_\lambda = 99, 199, 373$ and 448 . While there is a trend towards becoming horizontal with R_λ , there is still a significant slope at the highest Reynolds number. The dashed lines show the accepted value of the Kolmogorov constant. It falls approximately midway between the low and high ends of the scaling range.

The spectra of figure 9(a) show, then, that while there clearly is a scaling region, its slope is not $-5/3$ even for the highest R_λ . It appears that the spectra are not yet self-similar. In order to describe them, we use a modified similarity form similar in approach to Sreenivasan (1991):

$$F_{11}(k_1) = C_{1*} \varepsilon^{2/3} k_1^{-5/3} (k_1 \eta)^{5/3-n_1}, \quad (13)$$

$$F_{22}(k_1) = C_{2*} \varepsilon^{2/3} k_1^{-5/3} (k_1 \eta)^{5/3-n_2}, \quad (14)$$

where n_1 and n_2 are the slopes of the scaling region for the u and v spectra respectively and C_{1*} and C_{2*} are now Kolmogorov variables: both C_* and n are functions of R_λ (and as $R_\lambda \rightarrow \infty$, $n_1, n_2 \rightarrow 5/3$ and $C_* \rightarrow C$, equations (1) and (2)). In figure 9(b) we have plotted $C_{1*} = F_{11}(k) \varepsilon^{-2/3} k_1^{n_1} \eta^{n_1-5/3}$ vs. $k_1 \eta$ for the four spectra of figure 9(a). The value of n_1 , which varied from 1.40 ($R_\lambda = 99$) to 1.58 ($R_\lambda = 448$) was determined by trial and error such that the scaling region would be horizontal. Note that C_{1*} decreases as R_λ increases but even for the high- R_λ case its value is approximately 0.7, well above the accepted high-Reynolds-number estimate of approximately 0.5 (Monin & Yaglom 1975; Sreenivasan 1995). Before we look at the evolution of C_* we will examine the way the slope of the spectra varies with R_λ .

Figure 10(a) is a summary of the best-fit scaling exponent, n_1 , for all the u spectra we measured over the range $50 < R_\lambda < 473$. For low R_λ , we have used some of our conventional (static) grid data. Both the synchronous and random modes of running the grid have been included. In figure 10(b) we have plotted the same data as 10(a) as a function of R_λ . We have also included the low-Reynolds-number static grid data of Jayesh, Tong & Warhaft (1994, figure 7). Finally in figure 10(c) we have plotted the slope of the transverse spectra, n_2 , as a function of R_λ .

The results of figure 10(a,b) show that below $R_\lambda \sim 100$ ($R_\lambda \sim 600$) the spectra have a scaling region in the range 1.3 to 1.4. The relatively large uncertainty is due to the small width of the scaling region. (Below $R_\lambda \sim 50$ no scaling region could be discerned at all (Jayesh *et al.* 1994).) There is then a relatively well-defined transition region extending from $R_\lambda \sim 100$ to $R_\lambda \sim 200$ where the scaling exponent steepens to a value of about 1.52. Beyond $R_\lambda \sim 200$ the slope tends to increase very slightly. Our maximum slope was 1.58 at $R_\lambda \sim 473$. We emphasize the high degree of reproducibility of the high-Reynolds-number experiments ($R_\lambda > 250$). The experimental scatter was ± 0.01 .

The transverse, v , spectra (figure 10c) follow a similar trend to that of u but the slope at a particular R_λ is less and it corresponded to a shorter scaling region. This is consistent with the spectra of S & V (e.g. their figure 12). Note, here too, the rapid change of spectral slope up to $R_\lambda \sim 200$.

In figures 10(a) and 10(c) we have fitted curves (which were empirically described well by $-2/3$ power laws) to the u and v spectral exponents, n_1 and n_2 . Defining $p_1 = 5/3 - n_1$ and $p_2 = 5/3 - n_2$, we find

$$p_1 = 5.25 R_\lambda^{-2/3} \quad (15)$$

and

$$p_2 = 7.51 R_\lambda^{-2/3}. \quad (16)$$

These $-2/3$ power laws suggest that a $5/3$ scaling region (to within a measurement error of 0.01) will not occur until $R_\lambda \sim 10^4$. We will show below that this is consistent with recent high- R_λ measurements done in large wind tunnels and in the atmosphere.

We now return to the value of the Kolmogorov constant. Figure 11 shows a plot of C_{1*} and C_{2*} as a function of p . (The values of C_* were determined from all of the measured spectra in the same manner as for the four spectra in figure 9(b).) The best fit line to C_{1*} is

$$C_{1*} = 0.51 + 2.39 p_1. \quad (17)$$

Thus, when $p_1 = 0$ ($n_1 = 5/3$), $C_{1*} = C_1 = 0.51$. The generally accepted value of the three-dimensional Kolmogorov constant C is 1.5 (e.g. Monin & Yaglom 1975) and the one- and three-dimensional constants are related by $C_1 = 18C/55$. Thus

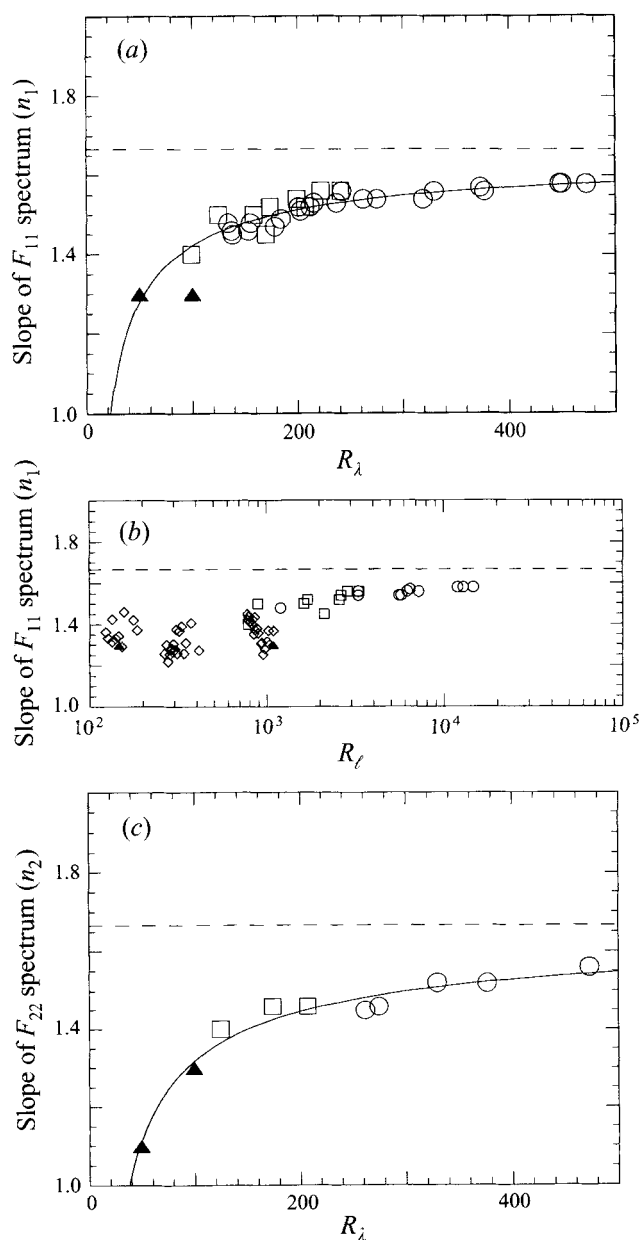


FIGURE 10. The slope, n_1 , of the $F_{11}(k_1)$ spectrum, (a, b), and the slope, n_2 , of the $F_{22}(k_1)$ spectrum, (c), as a function of Reynolds number. In (a) and (c) n_1 and n_2 respectively are plotted as a function of R_λ while in (b), n_1 is plotted as a function of R_ℓ . Open circles and squares are random and synchronous modes respectively. Solid triangles are for a conventional grid. The open diamonds (b only) are from conventional grid data of Jayesh *et al.* (1994). In (b), R_ℓ has been determined directly from the peaks of the $k_1 F_{11}(k_1)$ spectra and thus there is not a precise correspondence with each point on (a) using the fit $R_\ell = 0.06(R_\lambda)^2$ (equation (10)).

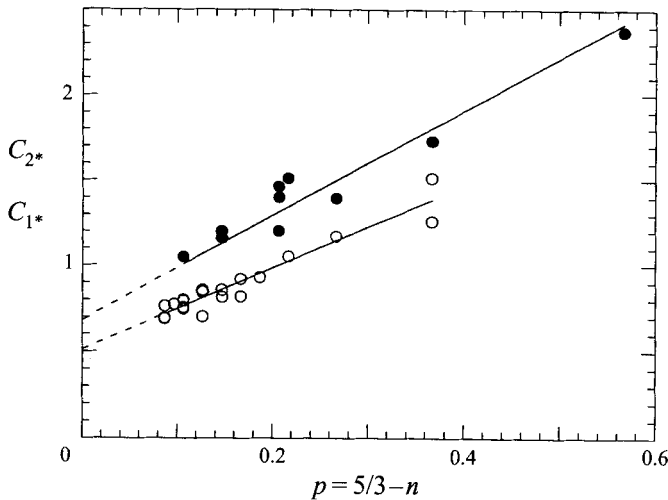


FIGURE 11. C_{1*} (open circles) and C_{2*} (closed circles) (equations (13) and (14)) plotted as a function of $p = 5/3 - n$ where n is the slope of the respective spectrum. For C_{1*} , the line is that of best fit. For C_{2*} , the best fit line has been forced through $C_{1*}(p=0) \times 4/3$ at $p=0$.

$C_1 \approx 0.49$. Our extrapolated value of 0.51 is remarkably consistent with this value. We emphasize that equation (17) is a best fit.

The ratio of the Kolmogorov constants C_2/C_1 must be $4/3$ if $n_1 = n_2 = 5/3$. In order to determine the best fit line for C_{2*} we have used the value $C_2 = 4/3 \times 0.51$ for $p_2 = 0$ yielding

$$C_{2*} = 0.68 + 3.07p_2. \quad (18)$$

Finally, the dependence between C_* and R_λ can be determined by substituting equations (15) and (16) into (17) and (18):

$$C_{1*} = 0.51 + 12.6R_\lambda^{-2/3}, \quad (19)$$

$$C_{2*} = 0.68 + 23.1R_\lambda^{-2/3}. \quad (20)$$

Figure 12 shows a plot of C_{1*} and C_{2*} as a function of R_λ with the fitted curves (equations (19) and (20)). We have also included C_{1*} determined from the data of S & V. These data will be discussed in §5.

We now turn to the issue of isotropy. Assuming our flow is axisymmetric (the w statistics were determined to be the same as the v statistics), the isotropy is determined by the ratio of the u and v statistics. Figure 13 shows $F_{22}(k_1)/F_{11}(k_1)$, i.e. the ratio of the v to u spectra, for $R_\lambda = 50, 262$ and 377 . At small wavenumbers, this ratio should be 0.5 if the energy-containing scales are isotropic. Our ratios are smaller than this, reflecting the large-scale anisotropy discussed in §3. In the region for which our spectra exhibit power-law scaling (signified by arrows in figure 13) there is, at the higher Reynolds numbers, a significant wavenumber region for which the ratio of the spectra is approximately $4/3$, the value that must occur if both the u and v spectra have slopes of $-5/3$ and the turbulence is locally isotropic (this is the ratio C_2/C_1 , equation (1)). The width of the $4/3$ region is approximately one decade for the highest R_λ . For higher wavenumbers (the dissipation range), the ratio $F_{22}(k_1)/F_{11}(k_1)$ must increase as the spectra roll off exponentially and our spectra show this. (Noise appears to be limiting the upper and lower spectra at $k_1\eta \sim 0.5$.)

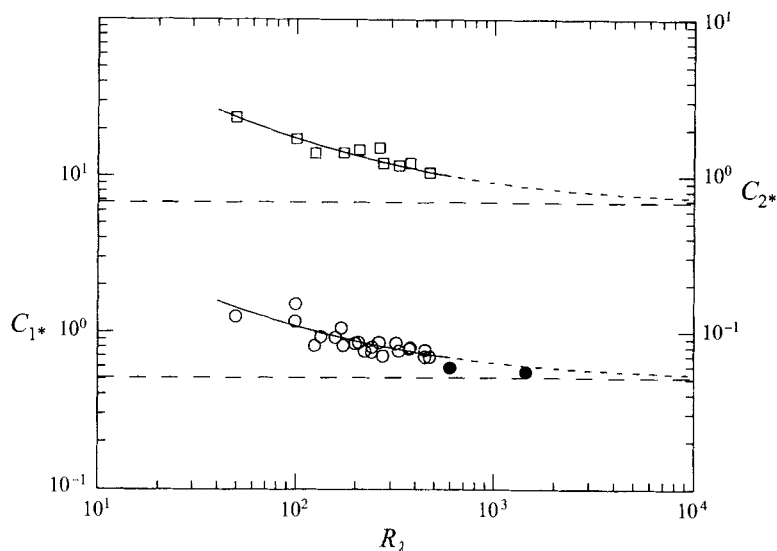


FIGURE 12. C_{1*} (open circles) and C_{2*} (open squares) as a function of R_λ . The curve fits are equations (19) and (20). The two closed circles are from S & V (see §5) and the dashed lines are the asymptotic limits of C_{1*} and C_{2*} .

Further insight into local isotropy in the inertial subrange can be gained by examining the ratio C_{2*}/C_{1*} . From equations (13) and (14) this is

$$C_{2*}/C_{1*} = [F_{22}(k_1)/F_{11}(k_1)](k\eta)^{n_2-n_1}. \quad (21)$$

Our experiments (figures 10(a, c)) show that $n_2 \neq n_1$. A plot of $n_1 - n_2$ is shown in figure 14. Since n_2 is always less than n_1 , equation (21) indicates that $F_{22}(k_1)/F_{11}(k_1)$ should increase with wavenumber and this is apparent for the lowest curve in figure 13. (We emphasize that this discussion holds for the scaling range only.) As R_λ increases, the slope of $F_{22}(k_1)/F_{11}(k_1)$ decreases (figure 13) since the difference between n_1 and n_2 diminishes. If $n_1 = n_2 = n$ then it can be shown from the isotropic relation between $F_{11}(k_1)$ and $F_{22}(k_1)$ (S. B. Pope, private communication), that

$$C_{2*}/C_{1*} = \frac{1}{2}(1 + n) \quad (22)$$

(yielding 4/3 for $n = 5/3$). For our high-Reynolds-number experiments $n_1 \sim n_2 \sim 1.6$ so $C_{2*}/C_{1*} \sim 1.3$ which cannot be experimentally differentiated from 1.33 (figure 13).

The ratio C_{2*}/C_{1*} (from the data of figure 12) is shown as a function of R_λ in figure 15. Notice that C_{2*}/C_{1*} (figure 15) is not equal to $F_{22}(k_1)/F_{11}(k_1)$ (figure 13), even for the high-Reynolds-number cases. Even here the small difference between n_1 and n_2 is significant and the relationship between C_{2*}/C_{1*} and $F_{22}(k_1)/F_{11}(k_1)$ must be determined from equation (21). Figure 15 suggests that the Kolmogorov value of 4/3 will be reached by $R_\lambda \sim 2200$. S & V comment that only for their highest R_λ case (of $R_\lambda = 1450$) do they see appreciable local isotropy. Our extrapolation is broadly consistent with their results.

In spite of the lack of complete similarity even at our highest R_λ , we have shown that all of our results are in agreement with the high-Reynolds-number scaling relationship $\ell/\eta \propto R_\lambda^{3/4}$ over the entire Reynolds number range (figure 7b). As stated in the Introduction, this law assumes that $\varepsilon \sim \langle u^2 \rangle^{3/2}/\ell$, i.e. that there is a cascade

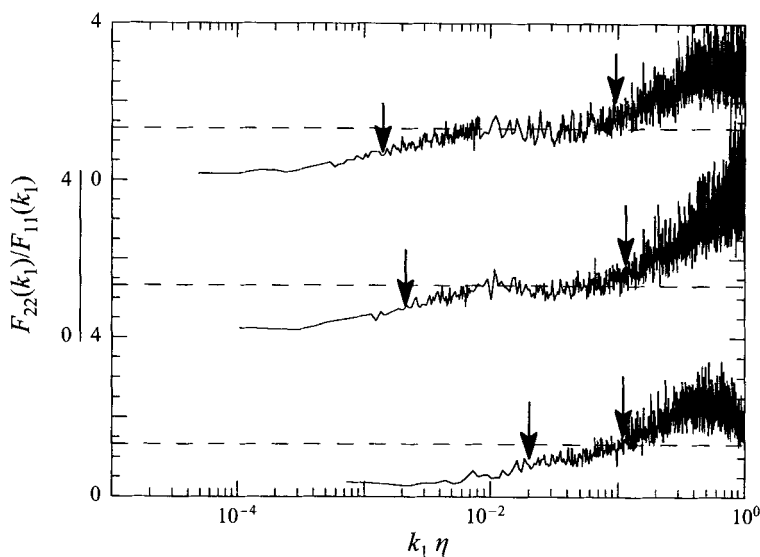


FIGURE 13. The ratio of the transverse to longitudinal spectra, $F_{22}(k_1)/F_{11}(k_1)$. The arrows mark the beginning and end of the $F_{11}(k_1)$ scaling range, i.e. the horizontal portion of the spectra when plotted in the manner of figure 9(b). The dashed line is the isotropic value of $4/3$. The bottom curve is for $R_\lambda = 50$ (done with a conventional grid). The middle curve ($R_\lambda = 262$) and top curve ($R_\lambda = 377$) were done with the active grid, random mode.

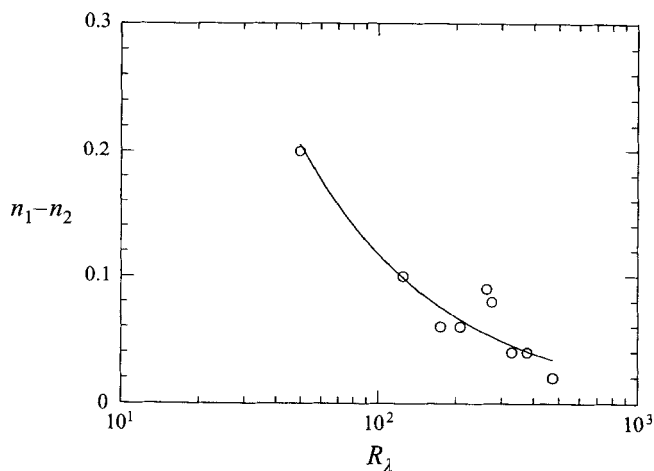


FIGURE 14. The difference between the longitudinal and transverse scaling exponents (n_1 and n_2 respectively) as a function of R_λ . The curve fit is $n_1 - n_2 = 4.7R_\lambda^{-4/5}$.

and that the (small scale) dissipation rate is determined by the large-scales. This in turn implies that there is a significant separation of scales. In order to provide a measure of the overlap between the integral and dissipation scales we integrated the $F_{11}(k_1)$ spectra and the $k_1^2 F_{11}(k_1)$ dissipation spectra (to be discussed further in §4.2). The results for R_λ of 99 and 448 are shown in figure 16. The data are represented so that for the energy spectrum the curve diminishes from unity to zero with increasing wavenumber, providing a measure of the ratio of energy above a particular wavenumber to the total amount for all wavenumbers. For the dissipation

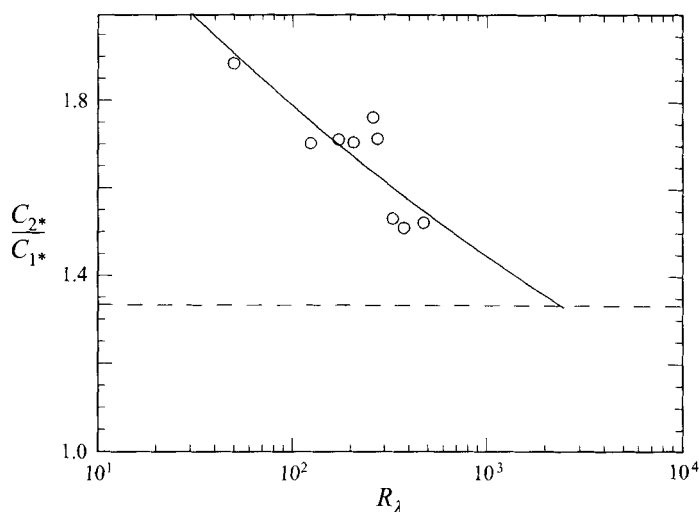


FIGURE 15. C_{2*}/C_{1*} as a function of R_λ . The curve fit is $C_{2*}/C_{1*} = 2.74R_\lambda^{-0.092}$. The horizontal line is $4/3$.

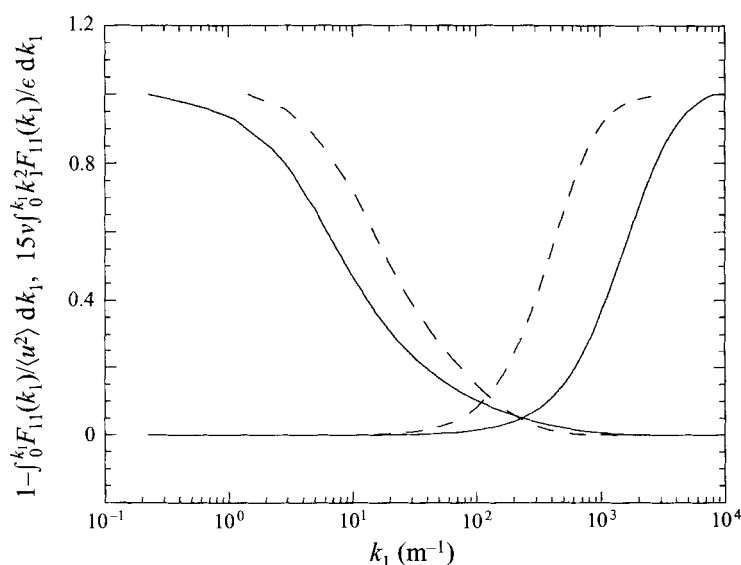


FIGURE 16. $1 - \int_0^{k_1} F_{11}(k_1)/\langle u^2 \rangle dk_1$ (curves decreasing with increasing k_1) and $15\nu \int_0^{k_1} k_1^2 F_{11}(k_1)/\epsilon dk_1$ (curves increasing with increasing k_1). The dashed curves are $R_\lambda = 99$ (synchronous mode). The solid curves are for $R_\lambda = 448$ (random mode).

spectra the curve is the ratio of the dissipation *below* a particular wavenumber to the total amount for all wavenumbers. Thus where the two curves cross, the proportion of energy from the integral scales overlapping with the dissipation scales is equal to the proportion of dissipation overlapping with the integral scales. We will call the value of this normalized integral I_c . It is a useful (but non-unique) indicator of the overlap.

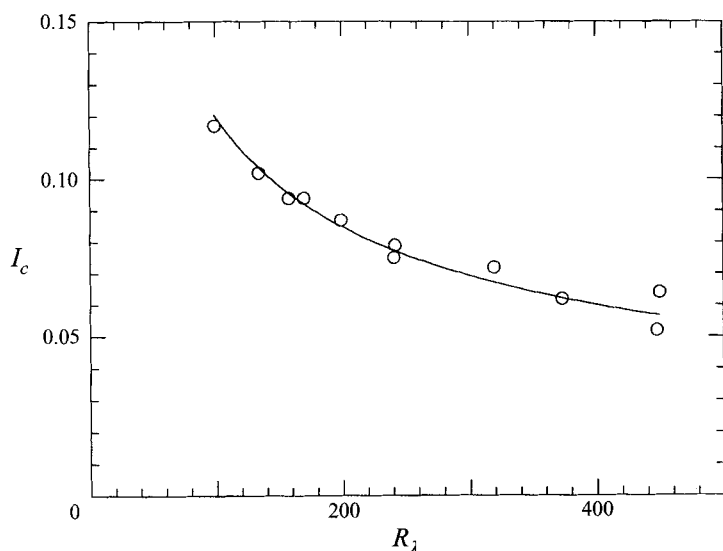


FIGURE 17. The value of I_c , the vertical ordinate (figure 16) where the energy and dissipation curves cross. The best fit curve is $I_c = 1.2 R_\lambda^{-1/2}$.

A plot of I_c vs. R_λ is shown in figure 17. As the two examples of figure 16 have already shown, its value decreases with R_λ , from about 0.11 at $R_\lambda \sim 100$ to 0.06 for $R_\lambda \sim 450$. A $-1/2$ power law fitted the data well, yielding

$$I_c = 1.20 R_\lambda^{-1/2}. \quad (23)$$

We note that above $R_\lambda \sim 300$ the dependence of I_c on R_λ is very weak. Here too, the variation in n was small (figure 10a, c). This is the region of strong or fully developed turbulence, to be more fully explored in the next section.

The scaling law (equation (11)) shows that the ratio of the integral to dissipation scales increases as $R_\ell^{3/4}$, or $R_\lambda^{3/2}$. Since ℓ and η are separated by the inertial subrange in high-Reynolds-number turbulence, this law implies that the scaling region itself should grow as $R_\lambda^{3/2}$. Figure 18 shows the width of the scaling region (calculated as $\log(f_2/f_1)$ where f_1 and f_2 are the lower and higher ends, respectively, of the scaling region in the frequency domain (Jayesh *et al.* 1994)), plotted as a function of R_λ . Although there is considerable scatter (due largely to the difficulty in accurately determining f_1), the data are consistent with a dilation rate proportional to $R_\lambda^{3/2}$. On the other hand, the scaling region of the low-Reynolds-number ($R_\ell < 1000$, $R_\lambda < 130$) spectra taken with a grid (Jayesh *et al.* 1994, figure 8) are not consistent with equation (11). There, the increase in the width of the scaling region was much slower than $R_\ell^{3/4}$. Jayesh *et al.* (1994) suggested that the weak scaling region (of slope around 1.3) observed for $R_\ell < 1000$ ($R_\lambda < 130$) implied a transient state. They were unable to study higher Reynolds numbers, but the present results confirm that this is indeed the case, with the strong turbulence occurring at slightly higher Reynolds numbers ($R_\lambda > 200$).

We conclude this section with a discussion of the third-order structure function, $\langle \Delta u(r)^3 \rangle$ where $\Delta u(r)$ is the longitudinal velocity difference in the longitudinal direction. Unlike the second-order structure function (or spectrum), the form of $\langle \Delta u(r)^3 \rangle$ is model independent. For high-Reynolds-number turbulence it follows directly from

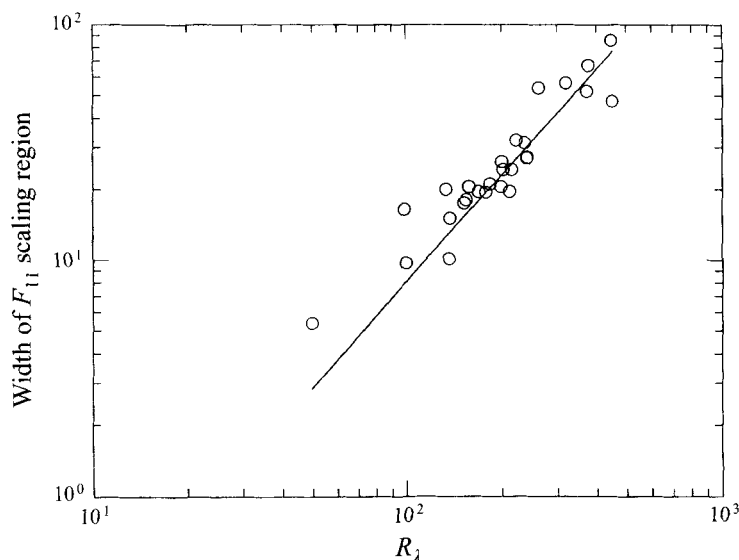


FIGURE 18. The width of the $F_{11}(k_1)$ scaling region as a function of R_λ . The line increases as $R_\lambda^{3/2}$.

the Navier-Stokes equations (Kolmogorov 1941*b*) that $\langle \Delta u(r)^3 \rangle = -(4/5)\epsilon r$. In figure 19 we have plotted $-\langle \Delta u(r)^3 \rangle / (r\epsilon)$ as a function of r/η for various R_λ . At high R_λ there should be a plateau at $4/5$. Our highest R_λ come close to this value although the plateau is not very wide. The quality of these structure functions is similar to that observed by Anselmet *et al.* (1984) for a jet at $R_\lambda = 536$. Our plots clearly show that for $R_\lambda < 150$ there is significant departure from the four-fifths law and this is consistent with our observations of the nature of the spectra in this region, a region which we have referred to as weak turbulence.

4.2. The p.d.f.s, conditional statistics and fine-scale structure

While approximately Gaussian at the large-scales, turbulence at the small scales is strongly intermittent and non-Gaussian. If the Reynolds number is high enough, the intermittent structure should be observable not only in the dissipation range, but also in the inertial subrange (K62). It is the main purpose of this section to show how the intermittent structure evolves with Reynolds number by studying the p.d.f.s and conditional statistics of inertial subrange quantities. But first we will document some of the derivative (dissipation) statistics.

Figure 20 shows the p.d.f.s of $\partial u / \partial t$ and $\partial v / \partial t$ at $R_\lambda = 262$. Both are super Gaussian. Their kurtoses ($K_{\partial u / \partial t}$ and $K_{\partial v / \partial t}$ defined as $\langle (\partial u / \partial t)^4 \rangle / \langle (\partial u / \partial t)^2 \rangle^2$ and similarly for $\partial v / \partial t$) are 7.3 and 9.7 respectively. The $\partial v / \partial t$ p.d.f. must have zero skewness ($S_{\partial v / \partial t} \equiv \langle (\partial v / \partial t)^3 \rangle / \langle (\partial v / \partial t)^2 \rangle^{3/2}$ and similarly defined for $\partial u / \partial t$) by symmetry. (Its measured value was 0.05.) However, $S_{\partial u / \partial t}$ must have skewness from purely kinematical considerations (e.g. Wyngaard & Tennekes 1970). Its value for the p.d.f. of figure 20 is 0.49. Figures 21(a) and 21(b) show plots of $S_{\partial u / \partial t}$, $K_{\partial u / \partial t}$ and $K_{\partial v / \partial t}$ as a function of R_λ . We have also included some high-Reynolds-number shear flow data taken from the compilation of Champagne (1978) as well as some low-Reynolds-number data from Tong & Warhaft (1994). The limited Reynolds number range and scatter of the present data are apparent from the graph, but the trend of the data (particularly for the kurtosis) as well as their magnitude is consistent with the shear flow data.

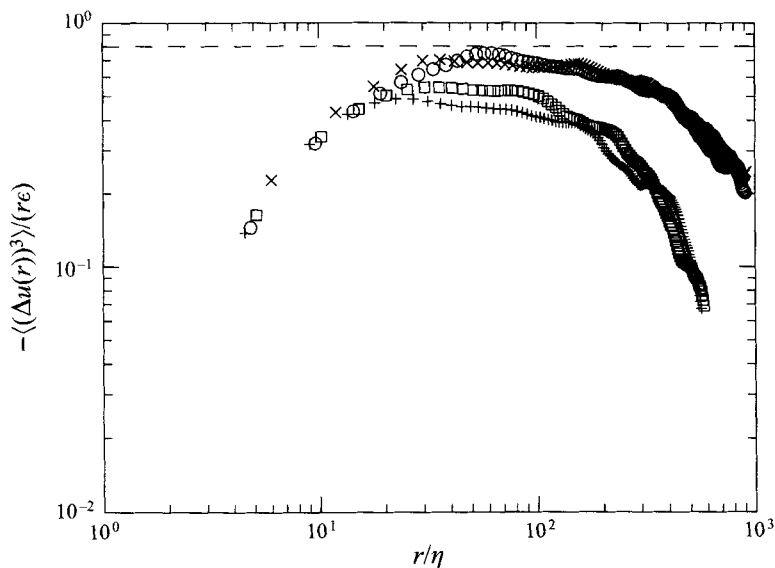


FIGURE 19. The compensated third-order structure function, $-\langle(\Delta u(r))^3\rangle/(r\epsilon)$. The symbols are: $+$, $R_\lambda = 99S$; \square , $R_\lambda = 134R$; \circ , $R_\lambda = 319R$; \times , $R_\lambda = 448R$. The dashed line is $4/5$.

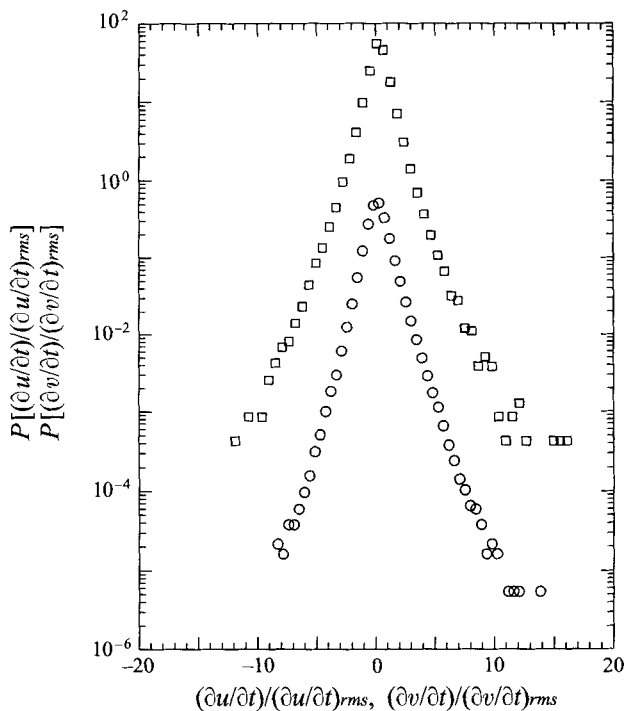


FIGURE 20. P.d.f.s of $\partial u/\partial t$ (circles) and $\partial v/\partial t$ (squares) for $R_\lambda = 262$. For $\partial u/\partial t$, S and K are 0.49 and 7.28 respectively. For $\partial v/\partial t$, S and K are 0.05 and 9.72 respectively. The curve for $\partial v/\partial t$ is shifted up by 2 decades.

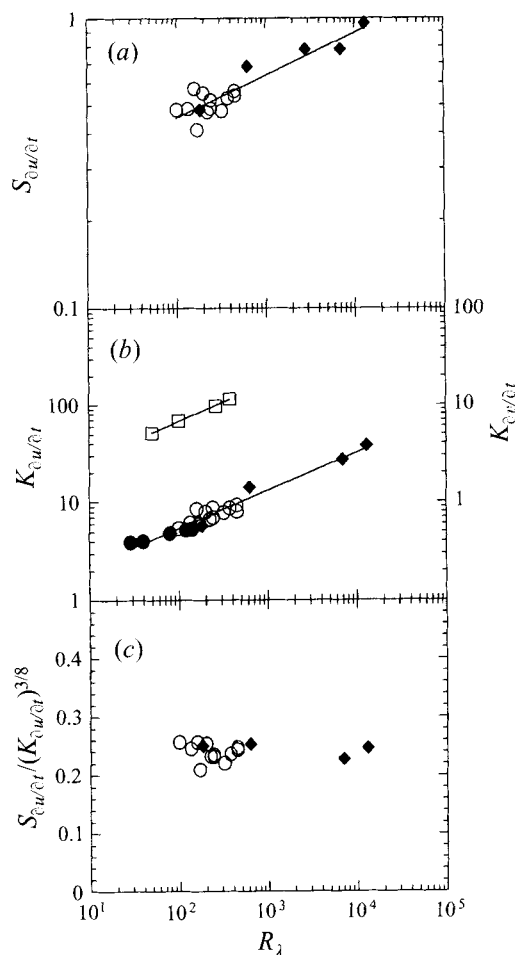


FIGURE 21. The skewness (a) and kurtosis (b) of the velocity derivatives as a function of R_λ . (c) The ratio $S_{\partial u / \partial t} / (K_{\partial u / \partial t})^{3/8}$. Open circles are for the present work. Closed diamonds are from shear flow data (Champagne 1978). Open squares are $K_{\partial v / \partial t}$, present work. Closed circles for $K_{\partial u / \partial t}$ are from Tong & Warhaft (1994).

Figure 21(c) shows the ratio $S_{\partial u / \partial t} / (K_{\partial u / \partial t})^{3/8}$. The data are again consistent with the shear flow data in which the ratio is not Reynolds-number dependent and is roughly equal to 0.25. It supports the prediction of Wyngaard & Tennekes (1970) that $S_{\partial u / \partial t} \propto (K_{\partial u / \partial t})^{3/8}$.

The ratio of the derivative variance, $\langle (\partial u / \partial t)^2 \rangle / \langle (\partial v / \partial t)^2 \rangle$, is given in table 1. Its value varies from 0.57 to 0.53. The isotropic value is 0.50. Thus our results suggest a small departure from isotropy at the dissipation scales. It is possible that this reflects the slight difference in inertial subrange dynamics for u and v (the values of the scaling exponents are different, figure 14). We note that the ratio is slowly tending to 0.5 with increasing R_λ .

In figure 22 we show the one-dimensional dissipation spectra for u and v determined by multiplying the power spectra by k_1^2 . The integral of these dissipation spectra yielded values of ε within a few percent of those determined using the u derivative. These spectra, for $R_\lambda = 377$ were typical: there appeared to be little variation with

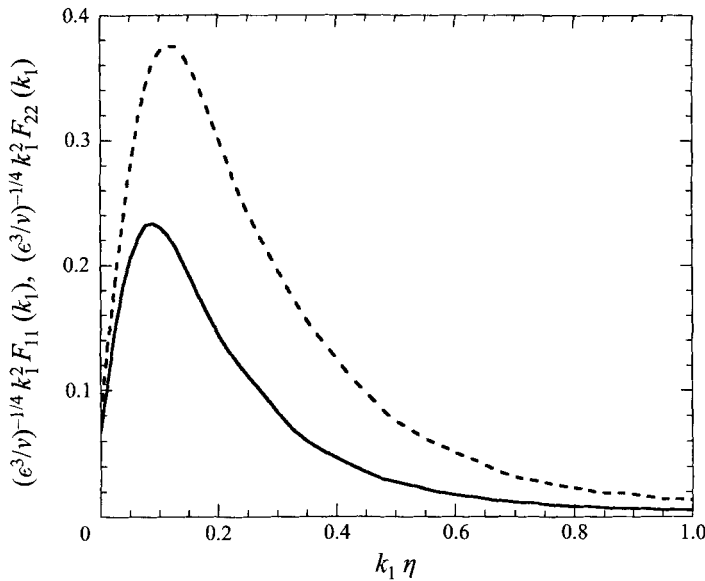


FIGURE 22. The dissipation spectra, $R_\lambda = 377$, random mode. The solid and dashed lines are the u and v dissipation spectra respectively.

R_λ . The scatter was around $\pm 5\%$ about an average value of 0.23 in the peak of the u dissipation spectrum over the range $100 < R_\lambda < 473$.

We now turn to the p.d.f. and conditional statistics of the velocity difference

$$\Delta u(r) = u(x+r) - u(x), \quad (24)$$

$$\Delta v(r) = v(x+r) - v(x), \quad (25)$$

where r is an inertial range distance. The behaviour of the statistics of Δu and Δv are central to understanding models of internal intermittency and thus form the basis for modifications to K41. Beginning with K62, there has been a vast literature on this subject, known as the Kolmogorov refined similarity hypothesis (KRSF). The subject is still in ferment. Reviews are given by Kraichnan (1991) and Nelkin (1994). More recent work will be referred to where appropriate.

For our highest and lowest values of R_λ (473 and 50 respectively) we varied r (equations (24) and (25)) across the whole of the scaling range. We will show that the statistics of $\Delta u(r)$ (as well as $\Delta v(r)$) are quite different for those two extreme Reynolds numbers. But in order to examine the trend of $\Delta u(r)$ and $\Delta v(r)$ as a function of Reynolds number, we chose a single value of r (denoted as r_a) corresponding to the wavenumber $k_1(r = 2\pi/k_1)$ that is halfway between the beginning and end of the scaling range (on a linear plot) for each spectrum. Thus as the scaling range dilates with Reynolds number, r_a remains in the same relative position within the scaling region. Figure 23 shows two spectra ($R_\lambda = 50$ and 473) with arrows pointing to the beginning and end of the scaling range as well as to the wavenumber corresponding to r_a . (For the low-Reynolds-number case, the scaling range is very slight indeed.) On some occasions we will also look at the statistics of $\Delta u(r)$ and $\Delta v(r)$ for larger r , chosen so that its value is midway between the beginning and end of the scaling region on the logarithmic plot. This is denoted as r_b in figure 23.

Figure 24 shows p.d.f.s of Δu and Δv , normalized by their respective r.m.s. values for the r_a separation. For the two lowest values of R_λ the p.d.f.s are close to Gaussian

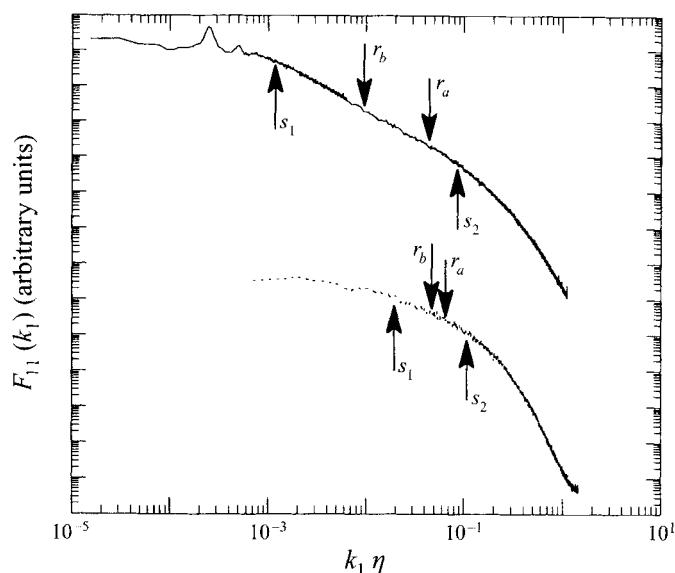


FIGURE 23. $F_{11}(k_1)$ spectra with the beginning and ends of the scaling region (s_1 and s_2 respectively) and the intervals r_a and r_b used for velocity difference statistics (see text) marked by arrows. Upper curve $R_\lambda = 473$ (random mode); lower curve $R_\lambda = 50$ (static grid).

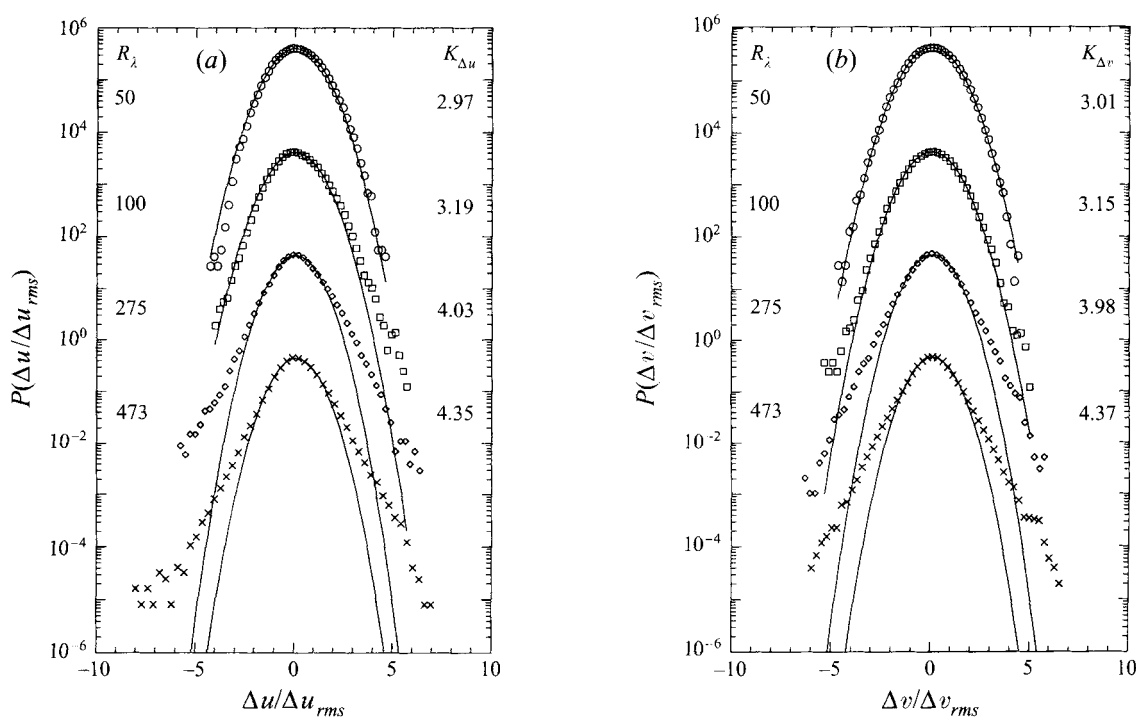


FIGURE 24. The p.d.f.s of $\Delta u(r_a)$ and $\Delta v(r_a)$, (a) and (b) respectively. The R_λ and kurtosis are labelled on the graph. Each graph has been shifted by 2 decades with respect to the lower one. The measurements for $R_\lambda = 50$ and 100 were done using a conventional static grid; for all other R_λ the active grid was in the random mode. The solid lines are Gaussian.

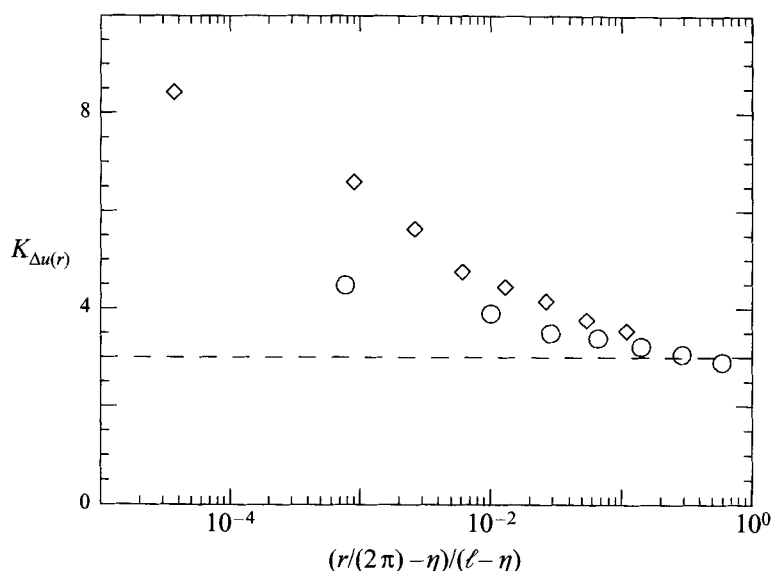


FIGURE 25. The kurtosis of the velocity difference as a function of r for $R_\lambda = 100$ (conventional grid) (circles) and 473 (active grid, random mode) (diamonds). The r normalization facilitates proper comparison of the two data sets.

but for the high R_λ cases there are significant tails on both the Δu and Δv p.d.f.s. The values of the kurtosis are listed on the graphs. The KRSH predicts that at high R_λ the p.d.f.s of the velocity differences should be super Gaussian due to the internal intermittency being reflected in the inertial subrange. Figure 24 suggests that high-Reynolds-number in this contexts means for R_λ greater than 100. We will show below that there is in fact a fairly distinct transition in the range $100 < R_\lambda < 200$.

Of course varying r changes the shape of the velocity-difference p.d.f.s: as r increases they should become more Gaussian in character, while for smaller r , as dissipation distances are approached, the p.d.f.s should look more like those of the derivatives. Thus as r increases, the kurtosis of Δu , $K_{\Delta u}$, should decrease. The variation of $K_{\Delta u}$ with r varied across the full extent of the inertial subrange is shown in figure 25 for $R_\lambda = 100$ and 473. For both cases the kurtosis approaches 3 as r approaches ℓ . For intermediate values of r , $K_{\Delta u}$ is lower for the low-Reynolds-number case and this is consistent with figure 24.

We now study the conditional statistics of Δu and Δv . K62 hypothesised that for high R_λ , the energy dissipation rate averaged over a radius r , ε_r , (where r is within the inertial subrange) is related to $\Delta u(r)$ by

$$\Delta u(r) = V(r\varepsilon_r)^{1/3} \quad (26)$$

where V is a stochastic variable independent of r and ε_r . Thus the quantities $\Delta u(r)$ and ε_r must be statistically dependent. In figure 26 we have plotted $(r_a\varepsilon_{r_a}^{11})^{1/3}$ and $(r_a\varepsilon_{r_a}^{21})^{1/3}$ conditioned on $\Delta u(r_a)$. Here $\varepsilon_{r_a}^{11}(\equiv 15\nu U^{-2}\langle(\partial u/\partial t)^2\rangle)$ and $\varepsilon_{r_a}^{21}(\equiv 7.5\nu U^{-2}\langle(\partial v/\partial t)^2\rangle)$ are (one-dimensional surrogates for the total dissipation) determined over a record of length r_a , from which we also obtained $\Delta u(r_a)$ from velocity difference between the start and end of the record. The data have been normalized by $(r_a\langle\varepsilon^{11}\rangle)^{1/3}$ (or $(r_a\langle\varepsilon^{21}\rangle)^{1/3}$) and are plotted as a function of $\Delta u(r_a)$ normalized by the r.m.s. value of $\Delta u(r_a)$. For high R_λ , figure 26 shows that both $\varepsilon_{r_a}^{11}$ and $\varepsilon_{r_a}^{21}$ are statistically dependent on $\Delta u(r_a)$:

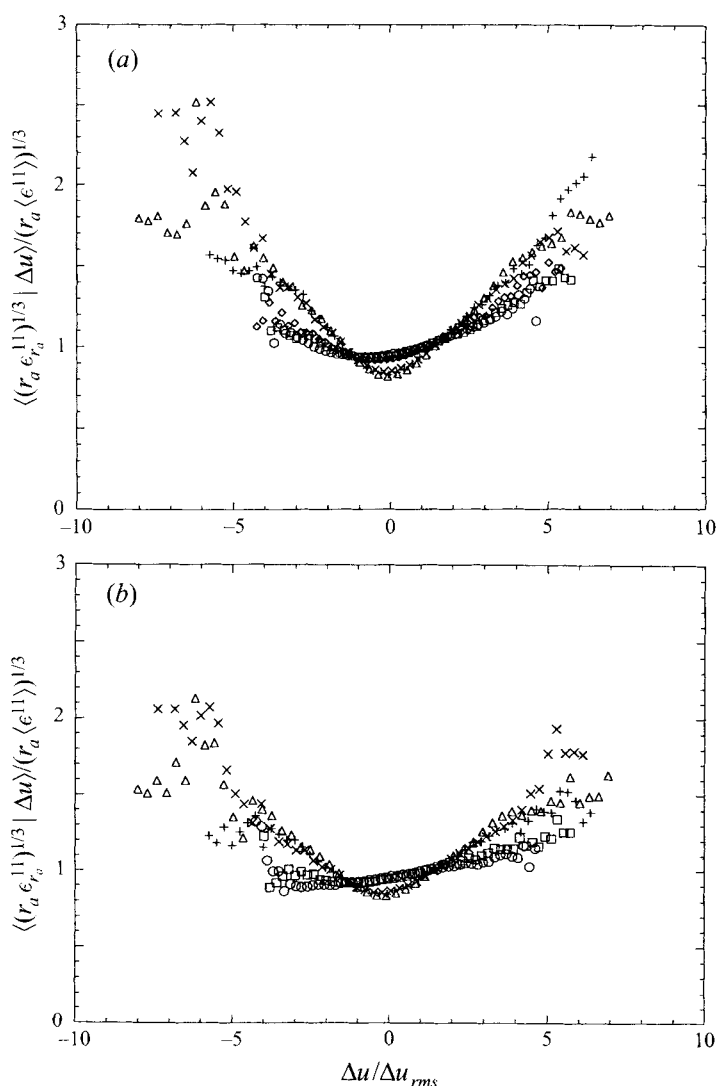


FIGURE 26. The expectation of $\epsilon_{r_a}^{11}$ conditioned on $\Delta u(r_a)$ and $\epsilon_{r_a}^{21}$ conditioned on $\Delta u(r_a)$. (a) $[(r_a \epsilon_{r_a}^{11})^{1/3} | \Delta u(r_a)] / (r_a \langle \epsilon^{11} \rangle)^{1/3}$, (b) $[(r_a \epsilon_{r_a}^{21})^{1/3} | \Delta u(r_a)] / (r_a \langle \epsilon^{21} \rangle)^{1/3}$. For both (a) and (b) the symbols are: \triangle , $R_\lambda = 473R$; $+$, $R_\lambda = 275R$; \times , $R_\lambda = 207S$; \diamond , $R_\lambda = 99S$; \square , $R_\lambda = 100$ (conventional grid, $M = 10.2$ cm), \circ , $R_\lambda = 50$ (conventional grid, $M = 2.54$ cm).

the curves have a pronounced V shape indicating that higher dissipation (averaged over r_a) is associated with larger velocity differences. For low R_λ , the conditional statistics are considerably flatter, showing only a weak dependence on $\Delta u(r_a)$. This is particularly so for the $\epsilon_{r_a}^{21}$ case (figure 26b). Notice the asymmetry in those curves for low R_λ . The only other determination of ϵ_r conditioned on $\Delta u(r)$ appears to be the numerical simulations of Chen *et al.* (1995) done up to a maximum R_λ of 212. They too observe the asymmetry. However, it is unclear what the precise correspondence between their R_λ and ours is. Notice also in figure 26 that for $R_\lambda \approx 100$ we have reported experimental results both for the active and static grids and these yield the same conditional expectations, showing consistency between the two different grids.

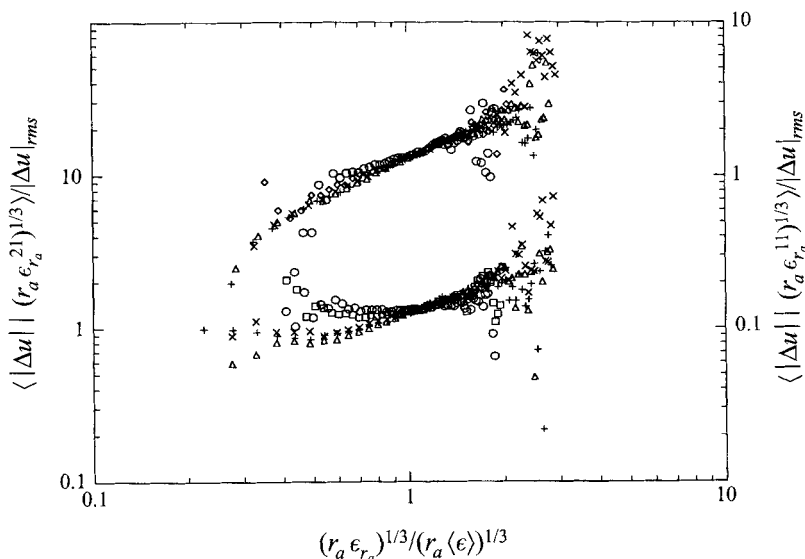


FIGURE 27. The expectation of $|\Delta u(r_a)|$ conditioned on $\varepsilon_{r_a}^{21}$ and $\varepsilon_{r_a}^{11}$. Lower curves (left-hand axis): $\langle |\Delta u(r_a)| | (r_a \varepsilon_{r_a}^{21})^{1/3} \rangle / |\Delta u|_{rms}$. Upper curves (right-hand axis): $\langle |\Delta u(r_a)| | (r_a \varepsilon_{r_a}^{11})^{1/3} \rangle / |\Delta u|_{rms}$. The symbols are the same as for figure 26.

Recently Chen *et al.* (1995) and Thoroddsen (1995) have pointed out that a statistical dependence between $\Delta u(r)$ and $r\varepsilon_r^{11}$ must occur, even if KRHS does not hold. A correlation will occur between ε_r^{11} and $\Delta u(r)$ on purely kinematic grounds. For a given $\Delta u(r)$, there exists a minimum possible value of the dissipation ε_r^{11} which corresponds to a linear variation in u over the distance r ($\varepsilon_r^{11}|_{\min} = 15\nu(\Delta u(r)/r)^2$). On the other hand, the existence of a statistical dependence between ε_r^{21} and $\Delta u(r)$ suggests a dynamical contribution. For our high- R_λ experiments (figure 26a, b) both ε_r^{11} and ε_r^{21} conditioned on $\Delta u(r)$ show statistical dependence on $\Delta u(r)$, giving strong support for KRHS.

In figure 27 we have plotted $|\Delta u(r_a)|$ conditioned on $\varepsilon_{r_a}^{11}$ and on $\varepsilon_{r_a}^{21}$. This type of conditional statistic has been previously determined experimentally (Stolovitzky, Kailasnath & Sreenivasan 1992; Praskovsky 1992; Zhu, Antonia & Hosokawa 1995; Thoroddsen 1995) and computationally (Chen *et al.* 1993; Wang *et al.* 1996) but has not been systematically studied over a wide range of Reynolds numbers. Note that there is not a simple correspondence between these and the conditional statistics of figure 26. Our results (figure 27) show that $|\Delta u(r_a)|$ conditioned on $\varepsilon_{r_a}^{11}$ shows similar statistical dependence on $\varepsilon_{r_a}^{11}$ for high and low Reynolds numbers suggesting that kinematics are largely responsible. However, $|\Delta u(r_a)|$ conditioned on $\varepsilon_{r_a}^{21}$, while showing statistical dependence for high R_λ , is nearly flat for the low- R_λ cases. Here the dynamical effects of the intermittency are evidently playing a role at high R_λ . This is consistent with figure 26(b). Thus the combination of our high- and low-Reynolds-number cases and the conditional statistics of both ε_r^{11} and ε_r^{21} on $\Delta u(r)$ enable us to separate the kinematical from the dynamical contributions to the statistical dependence: at low R_λ the dependence appears to be kinematical while at high R_λ a significant dynamical effect is observed. We note that recent data of Thoroddsen (1995) at $R_\lambda = 208$ shows independence of $\varepsilon_r^{21}(r)$ and $|\Delta u(r)|$. From this single observation, he casts doubt on KRSH. Our findings suggest his R_λ was probably not

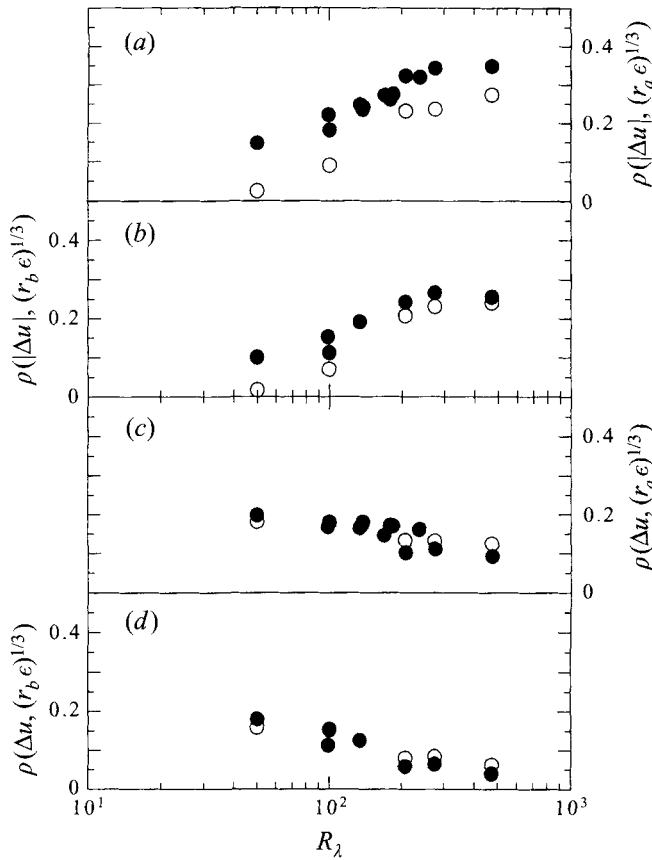


FIGURE 28. The correlation between the velocity differences $\Delta u(r_a)$ and $\Delta u(r_b)$ (and their modulus) and the dissipation computed over the same spatial interval, ε_r^{11} and ε_r^{21} (equations (27) and (28)), plotted as a function of R_λ . (a) $\rho_{|\Delta u(r)|, (r_a \varepsilon_r^{11})^{1/3}}$ (solid symbols) and $\rho_{|\Delta u(r)|, (r_a \varepsilon_r^{21})^{1/3}}$ (open symbols) for $r = r_a$. (b) Same as (a) but for $r = r_b$. (c) $\rho_{\Delta u(r), (r_a \varepsilon_r^{11})^{1/3}}$ (solid symbols) and $\rho_{\Delta u(r), (r_a \varepsilon_r^{21})^{1/3}}$ (open symbols) for $r = r_a$. (d) Same as (c) but for $r = r_b$.

quite high enough. The curves of figures 26 and 27 show that these quantities only tend to become dependent at around this value of R_λ .

The conditional statistics of $\Delta v(r)$ (not shown) were consistent with those of $\Delta u(r)$. Here $|\Delta v(r)|$ conditioned on ε_r^{11} showed statistical dependence at high R_λ while $|\Delta v|$ conditioned on ε_r^{21} showed statistical dependence for both high and low Reynolds numbers.

Figures 26 and 27 are for one value of r only. That the trends of these results (with R_λ) are not strongly dependent on the choice of r is shown in figure 28 where the cross-correlation coefficient between Δu (both its algebraic value and its modulus) and ε^{11} (and ε^{21}) defined as

$$\rho_{\Delta u(r), (r\varepsilon_r^{11})^{1/3}} = \langle (\Delta u(r) - \langle \Delta u(r) \rangle) (r\varepsilon_r^{11})^{1/3} - \langle (r\varepsilon_r^{11})^{1/3} \rangle \rangle / (\Delta u(r)_{rms} (r\varepsilon_r^{11})_{rms}^{1/3}) \quad (27)$$

and

$$\rho_{|\Delta u(r)|, (r\varepsilon_r^{11})^{1/3}} = \langle (|\Delta u(r)| - \langle |\Delta u(r)| \rangle) (r\varepsilon_r^{11})^{1/3} - \langle (r\varepsilon_r^{11})^{1/3} \rangle \rangle / (|\Delta u(r)|_{rms} (r\varepsilon_r^{11})_{rms}^{1/3}) \quad (28)$$

(and similarly for ε^{21}) is determined for both r_a and r_b (defined in figure 23). Both for

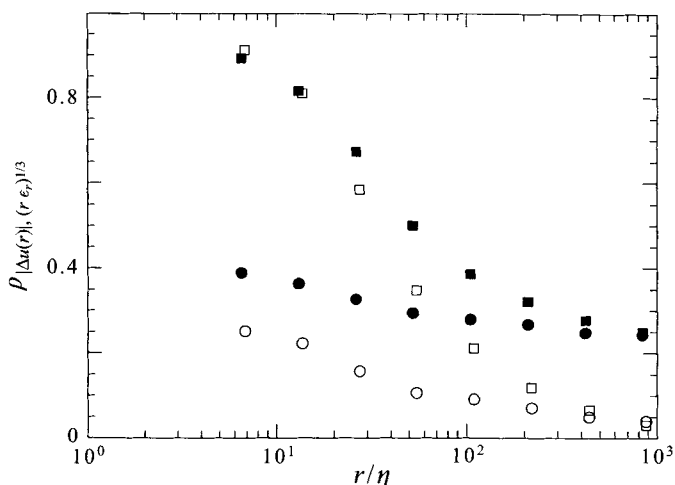


FIGURE 29. The cross-correlations $\rho_{|\Delta u(r)|, (r \varepsilon_r)^{1/3}}$ as a function of r/η for $R_\lambda = 473$ (solid symbols) and $R_\lambda = 100$ (open symbols). Squares: $\rho_{|\Delta u(r)|, (r \varepsilon_r^{11})^{1/3}}$; circles: $\rho_{|\Delta u(r)|, (r \varepsilon_r^{21})^{1/3}}$.

r_a and r_b the cross-correlation $\rho_{|\Delta u(r)|, (r \varepsilon_r^{11})^{1/3}}$ begins to become significant at $R_\lambda \sim 100$, reaching values of 0.35 and 0.25 for r_a and r_b respectively at $R_\lambda \sim 200$. The value of $\rho_{|\Delta u(r)|, (r \varepsilon_r^{21})^{1/3}}$ is close to zero for $R_\lambda < 100$ suggesting that the small correlation between $|\Delta u(r)|$ and ε_r^{11} for low R_λ is kinematical only. (Notice that the cross-correlation of $|\Delta u(r)|$ and ε_r^{11} is shifted down with respect to the cross-correlation of $|\Delta u(r)|$ and ε_r^{21} figure 28(a, b).) It is clear from these correlations that there is a significant change in the turbulence characteristics for $100 < R_\lambda < 200$. Over this interval there is a transition from weak turbulence (with almost Gaussian p.d.f.s of $\Delta u(r)$, figure 24, and weak statistical dependence between $\Delta u(r)$ and ε_r figures 26 and 27) to strong turbulence which exhibits non-Gaussian p.d.f.s and strong statistical dependence between $\Delta u(r)$ and ε_r . We observed in the section on spectra that there was also a distinct change in the nature of the spectrum over the same R_λ range.

The trends in $\rho_{\Delta u(r), (r \varepsilon_r)^{1/3}}$ are opposite to those of $\rho_{|\Delta u(r)|, (r \varepsilon_r)^{1/3}}$ (figure 28c, d) and their magnitudes are much smaller (due to the rapid oscillations of the sign of $\Delta u(r)$). Both of these observations are consistent with the recent estimates (of $\Delta u(r)$ correlated with ε_r^{11} only) by Zhu *et al.* (1995) who compare jet data ($R_\lambda \sim 250$) and atmospheric boundary layer data ($R_\lambda \sim 7200$).

The variation of $\rho_{|\Delta u(r)|, (r \varepsilon_r)^{1/3}}$ with r/η is shown in figure 29, for $R_\lambda = 100$ and 473. Notice that for $|\Delta u(r)|$ correlated with ε_r^{11} there is a rapid decrease (to zero) as r/η increases. This variation has also been observed by Praskovsky (1992) and by Zhu *et al.* (1995). On the other hand, for the high- R_λ case, the cross-correlation between $|\Delta u(r)|$ and ε_r^{21} declines relatively slowly, remaining almost constant (with a value of around 0.3) within the inertial subrange. Praskovsky (1992) points out (contrary to his own findings) that ρ_r should not depend on r within the inertial subrange for high-Reynolds-numbers. Our results show the importance of not using the same velocity component for $\Delta u(r)$ and ε_r .

Finally, we have determined the intermittency exponent (K62) from the autocorrelation of ε (Praskovsky & Oncley 1994; Nelkin 1994):

$$\rho_{\varepsilon\varepsilon}(r) = \frac{\langle \varepsilon(x)\varepsilon(x+r) \rangle}{\langle \varepsilon^2 \rangle} \propto r^{-\mu}. \quad (29)$$

Figure 30(a) shows $\rho_{\varepsilon\varepsilon}(r)$ for the one-dimensional surrogates ε^{11} and ε^{21} , plotted as a function of r/η for $R_\lambda = 100$ and 377. From these (and estimates at other R_λ), μ was determined by compensation, i.e. by multiplying $\rho_{\varepsilon\varepsilon}(r)$ by r^μ and adjusting μ so the curve became horizontal in the inertial range. These estimates of μ are plotted as a function of R_λ in figure 30(b). Below $R_\lambda \sim 100$, $\mu \sim 0$. This result is consistent with the nature of the velocity difference p.d.f.s (figure 24) and the conditional dissipation (figures 26 and 27) in this region. There is then a steep rise to a value of around 0.11 at $R_\lambda \approx 450$. Measurements in very high-Reynolds-number flows show that μ is approximately constant, with a value of approximately 0.2 (e.g. Praskovsky & Oncley 1994; Chambers & Antonia 1983). Evidently, we are not yet at a sufficiently high R_λ to attain this value. This is consistent with the spectra (§4.1) which are still evolving at $R_\lambda \sim 500$.

We point out that the curves in figure 30(a) appear to asymptote to a non-zero value at $r/\eta \rightarrow \infty$ (particularly at the lower R_λ where the inertial range ends at a lower value of r/η). The asymptotic value can be calculated by decomposition of the dissipation into mean ($\bar{\varepsilon}$) and fluctuating (ε') components as follows:

$$\begin{aligned} \lim_{r \rightarrow \infty} \rho_{\varepsilon\varepsilon}(r) &= \frac{\langle (\bar{\varepsilon}(x) + \varepsilon'(x))(\bar{\varepsilon}(x+r) + \varepsilon'(x+r)) \rangle}{\langle (\bar{\varepsilon} + \varepsilon')^2 \rangle} \\ &= \frac{\langle \bar{\varepsilon}(x)\bar{\varepsilon}(x+r) \rangle + \langle \varepsilon'(x)\varepsilon'(x+r) \rangle}{\langle \bar{\varepsilon}^2 \rangle + \langle \varepsilon'^2 \rangle} \\ &= \frac{\bar{\varepsilon}^2}{\bar{\varepsilon}^2 + \langle \varepsilon'^2 \rangle} \end{aligned} \quad (30)$$

The asymptotic limits of $\rho_{\varepsilon\varepsilon}(r)$, assuming $\bar{\varepsilon}(x) = \bar{\varepsilon}(x+r)$ (homogeneity) and $\lim_{r \rightarrow \infty} \langle \varepsilon'(x)\varepsilon'(x+r) \rangle = 0$ are indicated on figure 30(a).

The intermittency exponent provides the correction to K41, modifying the 5/3 scaling exponent to $5/3 + \mu/m$ where m is model dependent but is probably close to 9 (Nelkin 1994). Thus the slope of the spectrum is only slightly increased at high-Reynolds-numbers. Such a correction has not yet been observed. We will argue in the next section that this is because the R_λ must be greater than 10^4 , a value even larger than can be obtained from atmospheric measurements.

5. Discussion

Our experiments have shown that by $R_\lambda \sim 200$ the turbulence spectrum has a broad scaling range with a slope close to the Kolmogorov value of 5/3 and that the internal intermittency is well developed, showing interaction between the inertial and dissipation scales. As the Reynolds number is further increased the variation of the slope of the scaling exponent is only weakly dependent on R_λ .

How do these findings relate to other experiments done at much higher Reynolds numbers? An extrapolation of the scaling exponent, n_1 , (figure 10 and equation (15)) suggests that a true 5/3 exponent will not occur until $R_\lambda \sim 10^4$. At this value of R_λ we estimate C_1 (equation (1)) to be 0.51. Recently Praskovsky & Oncley (1994) have examined data from the atmosphere and from large wind tunnels in the R_λ range

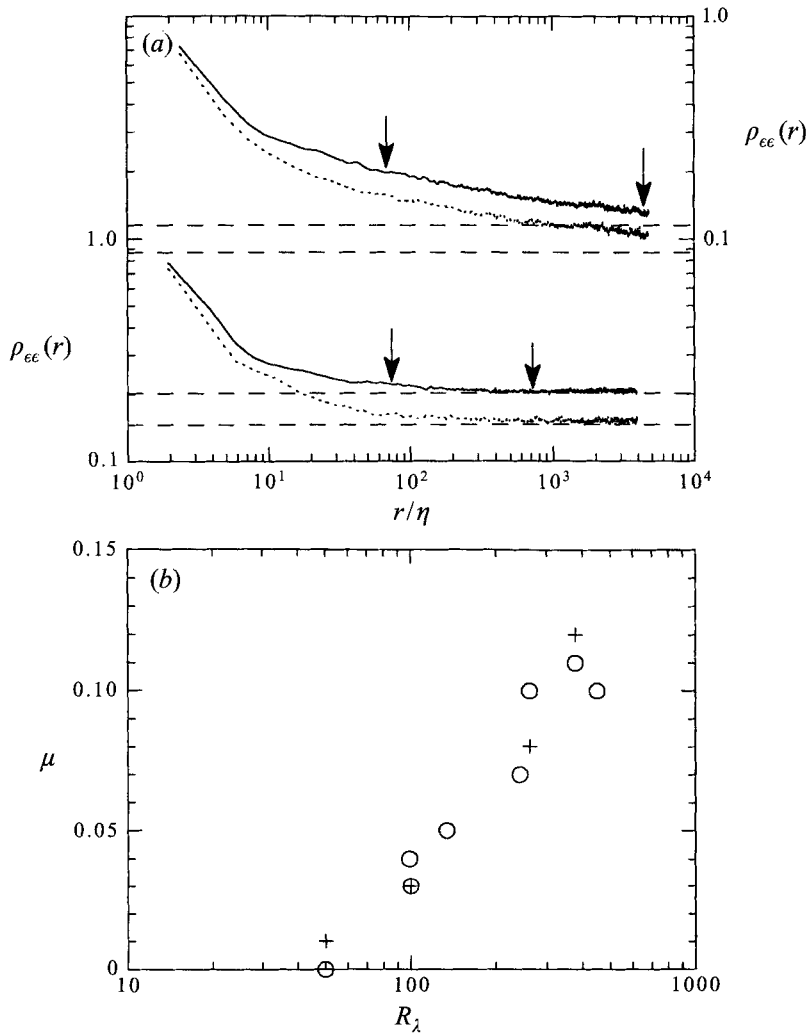


FIGURE 30. The estimate of μ using equation (29). (a) The auto correlation of ϵ^{11} (full line) and ϵ^{21} (dashed line). Lower curves are for $R_\lambda = 100$ (static grid); upper curves are for $R_\lambda = 377$ (active grid, random mode). The arrows signify the beginning and end of the scaling region. The horizontal lines are $\bar{\epsilon}^2/(\bar{\epsilon}^2 + \langle \epsilon'^2 \rangle)$ (see text). (b) μ determined from the slopes of $\rho_{ee}(r)$. Open circles are for ϵ^{11} ; plus signs are for ϵ^{21} .

10^3 to 10^4 . They do not find any measurable departure from $n = 5/3$ (our figure 10 suggests that at $10^3, n = 1.63$ a value very close to $5/3$). However, they find that C_1 (equation (1)) is not constant but has a small dependence on R_λ , varying from about $0.65(R_\lambda \sim 10^3)$ to $0.5(R_\lambda \sim 10^4)$. This result is remarkably consistent with an extrapolation of our results which show (figure 12) that at $R_\lambda \sim 10^4, C_{1*} = C_1 = 0.51$. (At $R_\lambda = 10^3$ our value of C_{1*} is 0.64 (figure 12 and equation (19)) but C_1 cannot be determined since the slope of the spectrum is still significantly different from $5/3$.)

The results of S & V also match well with our lower-Reynolds-number experiments. They show that not until $R_\lambda \sim 1500$ is there a significant inertial subrange. However, their plots of the compensated spectra (done in the same way as our figure 9a) show a slight increase with wavenumber. They attribute this to the so-called spectral bump

(near the dissipation range). We suggest that the scaling exponent has not quite reached $5/3$. We have calculated C_{1*} from their data (by replotting their spectra in the manner of our figure 9b). Its value is plotted in figure 12 and is consistent with the trend in our own data.

It appears, then, that an R_λ of approximately 10^4 is required before the prediction of K41 is properly fulfilled in terms of the spectrum (equation (1)). Presumably, the value of R_λ must be significantly greater than this before the Kolmogorov (1962) intermittency correction (which steepens the slope even further) will be observable. We note that an R_λ of 10^5 in air implies (assuming an r.m.s. velocity of 1 m s^{-1}) an integral length scale of 10 km! However, we believe that insight into the value of intermittency will be gained from controlled experiments at $R_\lambda \sim 1000$. We are currently building a large active grid to achieve this.

While the comparatively wide Reynolds number range of this study has been facilitated by new developments in grid design, it is curious that there appear to be no systematic studies of the variation of the turbulence spectrum with R_λ for other flows such as jets and boundary layers. These are flows for which a wide range of Reynolds numbers can be achieved with existing technology. It could be anticipated that the evolution of the spectrum for these flows will be different to that described here. For instance, in oscillating grid turbulence (a flow in which a conventional grid oscillates in a quiescent fluid) the $5/3$ slope tends to occur at low R_λ , and as soon as a scaling region is observed. This is possibly because the turbulence undergoes more straining by the time it reaches the measuring point (Hunt & Vassilicos 1991). Similarly, for a passive scalar in conventional grid turbulence, a scaling region occurs earlier than for the velocity field (Jayesh *et al.* 1994). The nature of turbulence statistics appears to be sensitive to their mode of generation even to quite high-Reynolds-numbers. It still remains to be seen whether true universality is ever achieved between flows of different origin, although the results presented here show at least for second-order moments there appears to be a consistency between grid turbulence and shear flows at high R_λ .

Our results have implications for the modelling of turbulence at moderate Reynolds numbers and are therefore of practical importance. We have shown that even by $R_\lambda \sim 500$, C_{1*} is 0.7, a value significantly different from the asymptotic value of 0.5. A value of $R_\lambda = 500$ is relatively high in terms of industrial fluid mechanics. For example, the R_λ of turbulence in a commercial combustor is of this order. Large-eddy simulations usually model the inertial subrange assuming that its behaviour is independent of R_λ . We suggest that errors will accrue unless the Reynolds number dependence is accounted for in these and other modelling procedures.

6. Conclusions

Using the active grid design of Makita (1991) we have explored the evolution of grid turbulence with Reynolds number. We have shown that as R_λ is varied from 50 to nearly 500 there is a qualitative change in the nature of the turbulence. For $R_\lambda < 100$ it has a weak scaling range (none at all below $R_\lambda \sim 50$) and there is little or no effect of the intermittency on the inertial range. Nevertheless here, as for high R_λ , $\varepsilon \sim \langle u^2 \rangle^{3/2} / \ell$ implying a fully developed cascade in which the dissipation can be inferred from large-scale quantities. We call this weak turbulence. Above $R_\lambda \sim 200$ the scaling region is well developed with an exponent close to $5/3$. Here the internal intermittency is reflected in the inertial subrange. We call this strong turbulence and have shown that it has similar characteristics to the high-Reynolds-number turbulence

studied in shear flows and in the atmosphere. We find that the change from weak to strong turbulence occurs in the range $100 < R_\lambda < 200$. Here there is rapid change in the value of the scaling exponent as well as in the conditional and other statistics (figures 10, 24, 26 and 28).

Our experiment appears to be the first to bridge the gap between the low-Reynolds-number ($R_\lambda \sim 50$) laboratory studies of grid-generated turbulence which have provided so much insight into its kinematics and dynamics (Batchelor 1953; Comte-Bellot & Corrsin 1971) and the high-Reynolds-number experiments ($R_\lambda \sim 10^3$) done in the atmosphere and the oceans that have provided broad confirmation of K41 as well as estimates of the scaling and intermittency exponents, and the Kolmogorov constant (see Champagne 1978; and Nelkin 1994 for references to more recent experiments). We note that many turbulent flows of practical importance, such as in industrial mixers or machines, occur at the intermediate Reynolds numbers studied here.

Our results suggests that much can be learned about the behaviour of turbulence at high-Reynolds-numbers using a small wind tunnel. We note that the insights gathered from the atmospheric experiments as well as from the canonical experiments of Saddoughi & Veeravalli (1994) are costly and varying flow conditions is difficult. (Indeed control is impossible in the atmosphere.) Nevertheless, the R_λ of 500 achieved in the present experiment is still too low to explore the detailed structure of high- R_λ turbulence. We have shown that at this R_λ there is still a significant evolution in the value of C_{1*} and C_{2*} (figure 12), the scaling exponent is still less than the Kolmogorov value of $5/3$ (figure 10) and μ , the intermittency exponent, is still less than the observed high- R_λ value of 0.2 (figure 30). We are presently constructing a larger Makita style grid with the aim of achieving an R_λ of around 1000, to study statistics higher than those of second order, to which we have confined ourselves here.

We once again thank Mr E. P. Jordan who expertly constructed the grid. Dr Chenning Tong carried out some preliminary experiments and Professors S. B. Pope and E. D. Siggia provided advice as well as encouragement. We sincerely thank them. The work was supported by the Department of Energy (Basic Energy Sciences) whom we also thank.

Note added in proof: Recently we have constructed a larger version of the active grid, obtaining an R_λ of 800. The new results are entirely consistent with the trends reported here; for example, the slope of the u spectrum is 1.6, at $R_\lambda \sim 800$ and this is consistent with the trend in figure 10(a). These, and results of passive scalar mixing experiments in the same flow, are presently being prepared for publication.

REFERENCES

- ANSELMET, F., GAGNE, Y., HOPFINGER, E. J. & ANTONIA, R. A. 1984 High-order velocity structure functions in turbulent shear flows. *J. Fluid Mech.* **140**, 63–89.
- BATCHELOR, G. K. 1953 *The Theory of Homogeneous Turbulence*. Cambridge University Press.
- BROWNE, L. W. B., ANTONIA, R. A. & CHUA, L. P. 1989 Calibration of X-probes for turbulent flow measurements. *Exps. Fluids* **7**, 201–208.
- CHAMBERS, A. J. & ANTONIA, R. A. 1984 Atmospheric estimates of power law exponents μ and μ_θ . *Boundary Layer Met.* **28**, 343–352.
- CHAMPAGNE, F. H. 1978 The fine-scale structure of the turbulent velocity field. *J. Fluid Mech.* **86**, 67–108.
- CHEN, S., DOOLEN, S. D., KRAICHNAN, R. H. & SHE, Z.-S. 1993 On statistical correlations between

velocity increments and locally averaged dissipation in homogeneous turbulence. *Phys. Fluids A* **5**, 458–463.

- CHEN, S., DOOLEN, S. D., KRAICHNAN, R. H. & WANG, L.-P. 1995 Is the Kolmogorov refined similarity relation dynamic or kinematic? *Phys. Rev. Lett.* **74**, 1755–1758.
- COMTE-BELLOT, G. & CORRSIN, S. 1966 The use of a contraction to improve the isotropy of grid-generated turbulence. *J. Fluid Mech.* **25**, 657–682.
- COMTE-BELLOT, G. & CORRSIN, S. 1971 Simple Eulerian time correlation of full and narrow-band velocity signals in grid-generated ‘isotropic’ turbulence. *J. Fluid Mech.* **48**, 273–337.
- GAD-EL-HAK, M. & CORRSIN, S. 1974 Measurements of the nearly isotropic turbulence behind a uniform jet grid. *J. Fluid Mech.* **62**, 115–143.
- HUNT, J. C. R. & VASSILICOS, J. C. 1991 Kolmogorov’s contributions to the physical and geometrical understanding of small-scale turbulence and recent developments. *Proc. R. Soc. Lond. A* **434**, 183–210.
- JAYESH & WARHAFT, Z. 1992 Probability distribution, conditional dissipation, and transport of passive temperature fluctuations in grid-generated turbulence. *Phys. Fluids A* **4**, 2292–2307.
- JAYESH, TONG, C. & WARHAFT, Z. 1994 On temperature spectra in grid turbulence. *Phys. Fluids* **6**, 306–312.
- KISTLER, A. L. & VREBALOVICH, T. 1966 Grid turbulence at large Reynolds numbers. *J. Fluid Mech.* **26**, 37–47.
- KOLMOGOROV, A. N. 1941a The local structure of turbulence in incompressible viscous fluid for very large Reynolds numbers. *Dokl. Akad. Nauk. SSSR* **30**, 301–305 (referred to herein as K41).
- KOLMOGOROV, A. N. 1941b Dissipation of energy in locally isotropic turbulence. *Dokl. Akad. Nauk. SSSR* **32**, 16–18 (referred to herein as K41).
- KOLMOGOROV, A. N. 1962 A refinement of previous hypotheses concerning the local structure of turbulence in a viscous incompressible fluid at very high Reynolds numbers. *J. Fluid Mech.* **13**, 82–85 (referred to herein as K62).
- KRAICHNAN, R. 1991 Turbulent cascade and intermittency growth. *J. Fluid Mech.* **434**, 65–78.
- LESIEUR, M. 1990 *Turbulence in Fluids*, 2nd Edn. Kluwer.
- LING, S. C. & WAN, C. A. 1972 Decay of isotropic turbulence generated by a mechanically agitated grid. *Phys. Fluids* **15**, 1363–1369.
- MAKITA, H. 1991 Realization of a large-scale turbulence field in a small wind tunnel. *Fluid Dyn. Res.* **8**, 53–64.
- MAKITA, H. & SASSA, K. 1991 Active turbulence generation in a laboratory wind tunnel. *Advances in Turbulence 3* (ed. A. V. Johansson & P. H. Alfredsson). Springer.
- MAKITA, H., SASSA, K., IWASAKI, T. & IJIDU, A. 1987 *Trans. Japan Soc. Mech. Engng B* **53**, 3180. (In Japanese).
- MONIN, A. S. & YAGLOM, A. M. 1975 *Statistical Fluid Mechanics*, Volume 2. MIT Press.
- NELKIN, M. 1994 Universality and scaling in fully developed turbulence. *Adv. Phys.* **43**, 143–181.
- PRASKOVSKY, A. A. 1992 Experimental verification of the Kolmogorov refined similarity hypothesis. *Phys. Fluids A* **4**, 2589–2591.
- PRASKOVSKY, A. A. & ONCLEY, S. 1994 Measurements of the Kolmogorov constant and intermittency exponent at very high Reynolds numbers. *Phys. Fluids* **6**, 2886–2888.
- SADDOUGH, S. G. & VEERAVALLI, S. V. 1994 Local isotropy in turbulent boundary layers at high Reynolds number. *J. Fluid Mech.* **268**, 333–372 (referred to herein as S & V).
- SIRIVAT, A. & WARHAFT, Z. 1983 The effect of a passive cross-stream temperature gradient on the evolution of temperature variance and heat flux in grid turbulence. *J. Fluid Mech.* **128**, 323–346.
- SREENIVASAN, K. R. 1991 On local isotropy of passive scalars in turbulent shear flows. *Proc. R. Soc. Lond. A* **434**, 165–182.
- SREENIVASAN, K. R. 1995 On the universality of the Kolmogorov constant. *Phys. Fluids* **7**, 2778–2784.
- STOLOVITZKY, G., KAILASNATH, P. & SREENIVASAN, K. R. 1992 Kolmogorov’s refined similarity hypotheses. *Phys. Rev. Lett.* **69**, 1178–1181.
- THORODDSEN, S. T. 1995 Reevaluation of the experimental support for the Kolmogorov refined similarity hypothesis. *Phys. Fluids* **7**, 691–693.
- TONG, C. & WARHAFT, Z. 1994 On passive scalar derivative statistics in grid turbulence. *Phys. Fluids* **6**, 2165–2176.

- TOWNSEND, A. A. 1976 *The Structure of Turbulent Shear Flow*, 2nd Edn. Cambridge University Press.
- WANG, L., CHEN, S., BRASSEUR, J. G. & WYNGAARD, J. C. 1996 Examination of hypotheses in the Kolmogorov refined turbulence theory through high-resolution simulations. Part 1. Velocity field. *J. Fluid Mech.* **309**, 113–156.
- WYNGAARD, J. C. 1968 Measurements of small-scale turbulence structure with hot wires. *J. Sci. Instrum.* **1**, 1105–1108.
- WYNGAARD, J. C. & TENNEKES, H. 1970 Measurement of the small scale structure of turbulence at moderate Reynolds numbers. *Phys. Fluids* **13** 1962–1969.
- YOON, K. & WARHAFT, Z. 1990 The evolution of grid-generated turbulence under conditions of stable thermal stratification. *J. Fluid Mech.* **215**, 601–638.
- ZHU, Y., ANTONIA, R. A. & HOSOKAWA, I. 1995 Refined similarity hypotheses for turbulent velocity and temperature fields. *Phys. Fluids* **7**, 1637–1648.